J. Fluid Mech. (1974), *vol.* 63, *part* 2, *pp.* 369–413
Printed in Great Britain

Experiments on the behaviour of an axisymmetric turbulent boundary layer with a sudden circumferential strain

By L. R. BISSONNETTE† AND G. L. MELLOR

Department of Aerospace and Mechanical Sciences,
Princeton University, New Jersey 08540

(Received 16 September 1971 and in revised form 30 July 1973)

Mean velocity and mean turbulent field measurements are performed for the case of a three-dimensional turbulent boundary layer on an axially rotated cylinder. The cylinder model consists of two parts: a stationary section followed by a spinning afterbody. Techniques of hot-wire anemometry are employed, which yield complete mean velocity and turbulence measurements in skewed flows. The general behaviour of the three-dimensional boundary layer is first discussed: two asymptotic layers analogous to the two-dimensional wall and defect layers are observed; they are shown to evolve from the equations of mean motion. The hypothesis of scalar eddy viscosity is investigated in the light of these results. Using conventional length scale assumptions together with the Reynolds stress tensor equations, a prediction of curvature effects in the law of the wall region is developed; a result in the present case is a smaller slope of the semi-logarithmic portion of the law of the wall. No assumptions over and above those necessary for plane, two-dimensional flow are required for this analysis. The geometry of the model is such that a rapid change in mean rate of strain occurs along the streamlines. From the history of the components of the $\overline{u_i u_j}$ tensor, it is possible to draw some fundamental conclusions concerning the dynamics of the energy dissipation, diffusion and redistribution processes.

1. Introduction

Turbulent boundary-layer theories have to date been derived almost exclusively from two-dimensional flow data. Theories founded on the simple mixing length or eddy viscosity hypothesis have achieved remarkable success in this field. Yet the very concept of eddy viscosity has long been questioned, especially the dependence of the mixing length or eddy transport on local mean flow conditions only. Furthermore, the basic eddy viscosity concept does not seem to evolve from the equations of motion. Consequently, researchers have recently been considering a variety of closure schemes for the mean turbulent field equations, which are physically more satisfying, but still require modelling of very important turbulent transport processes.

Three-dimensional flows are interesting because they constitute a serious test

---

† Present address: Defence Research Establishment Valcartier, Canada.

for theories that might work very well in most cases of two-dimensional flows, but whose shortcomings, if they exist, may be more visible in three-dimensional problems. The data offered here should be useful in challenging various turbulent boundary-layer models. Another feature of the present study is the experimental observation of the turbulence response to a rapidly changing mean rate of strain, which is intimately connected with the physics of the different turbulent transport processes, and thus should serve as a useful guideline for the constitutive hypotheses of any closure theory.

The geometry chosen for the present experiment is an axisymmetric turbulent boundary layer skewed by an axially rotated cylinder. Complete mean velocity and turbulence measurements were performed. A similar experiment was conducted by Furuya, Nakamura & Kawachi (1966), but they did not report turbulence measurements. Other types of three-dimensional boundary layers were studied by, for example, Johnston (1960), Hornung & Joubert (1963), Perry & Joubert (1965), Cham & Head (1969, 1970), but all these studies lack turbulence data. The only data of this sort (known to the authors) are due to Bradshaw & Terrell (1969) and Johnston (1970). In the former, the decay of weak crossflows under the action of shear stress alone was studied. In the latter, three-dimensionality was induced by a swept, forward-facing, step placed on a flat plate. The inconvenience of this type of geometry, as pointed out by the author, is that the flow is strongly influenced by pressure gradients, which certainly may conceal important aspects of the interaction between turbulent stresses and mean velocity field. In contrast, the present experiment involves fairly strong three-dimensional flows caused by the action of shearing stresses alone.

The cylinder model is made of two sections. The leading stationary section is immediately followed by a rotating section, so that fluid particles, as they enter the zone of influence of the rotating wall, are subjected to a relatively sudden change in mean rate of strain. Subsequently, an equilibrium axisymmetric turbulent boundary layer develops. From the history of each component of the $\overline{u_i u_j}$ tensor, some information can be drawn concerning the dynamics of turbulence. An analogy is the problem of the 'step' response of a given electronic circuit. In a related problem, Townsend (1954) devised an experiment to verify some of the predictions contained in a linearized theory first derived by Ribner & Tucker (1952) and later reconsidered by Batchelor & Proudman (1954). The experiment consisted of passing homogeneous turbulence through a constant-area distorting duct. Townsend found that the linear theory had some qualitative values only in the very early stages of the distortion, suggesting that nonlinear interaction was almost as fast as the distortion itself. Also, using a linearized set of equations, Moffatt (1965) showed that turbulence response to rapidly applied uniform shear is of viscoelastic form. The present method follows this line of thought. Although the situation is more complex owing to the geometry of the flow, fundamental features of the dynamics of turbulence can nevertheless be observed.

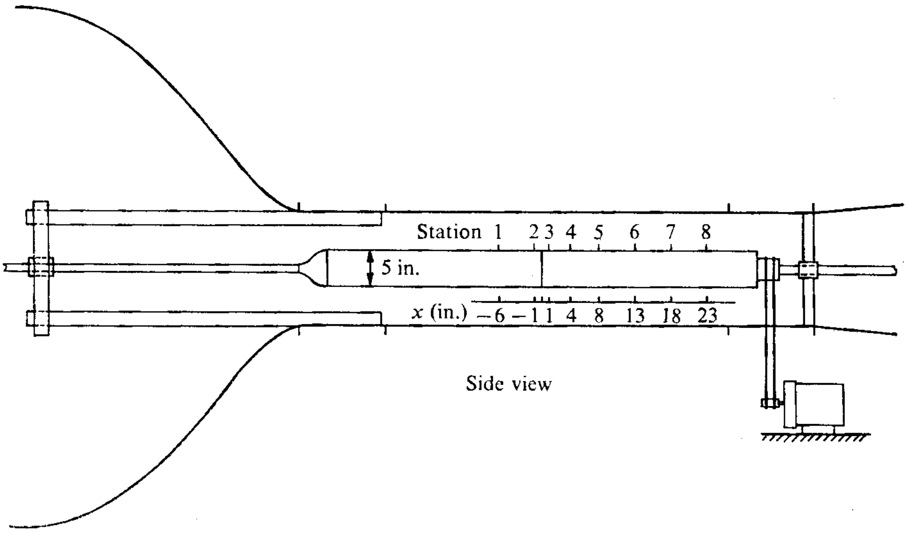

FIGURE 1. Schematic diagram of wind tunnel and model.

2. Experiment and apparatus

The experiment consisted of measuring the characteristics of the turbulent boundary layer that develops on a circular cylinder aligned with the mainstream. The cylinder was made of polished aluminum tubing 5 in. O.D. and 0·5 in. thick. It was mounted on a 10 ft long ground-steel shaft, rigidly supported at both ends. To minimize disturbances, the forward support was moved upstream, inside the settling chamber.

The model itself was made of two principal sections, each 2·5 ft long. The leading section was stationary, whereas the downstream section was mounted on ball bearings. The gap between the two sections was estimated at 0·002–0·003 in. The rotating cylinder was belt-driven from outside by a $\frac{1}{4}$ h.p. constant speed a.c. motor. The rotation speed was measured and constantly monitored by means of a strobe light. It was held constant for all cases reported here and its value was 2800 ± 25 rev/min.

The experiment was carried out in an open return wind tunnel. Figure 1 is a schematic drawing showing the model in place. The air entered through a bell-mouth and passed through seven 24-mesh gauzes and a short settling length before a 20:1 ratio, axisymmetric contraction. The working section was circular, 16 in. in diameter and 6 ft long. The air then passed through a diffuser before being exhausted into the atmosphere by an axial flow fan driven by a 5·3 h.p. d.c. motor. The air speed could be varied continuously between approximately 10 and 65 ft s^{-1}.

Because of the large contraction ratio of the entrance nozzle, disturbances created by the forward support should be sufficiently reduced. The mainstream turbulence level, with the model in place, was measured to be less than 0·5 %. This is not impressively small, but still small enough compared with boundary-layer generated turbulence.

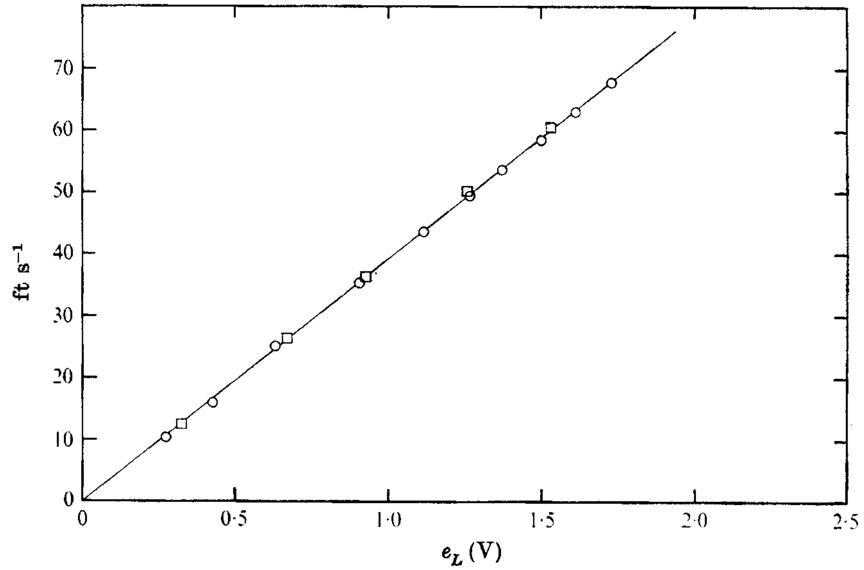

FIGURE 2. Sample calibration curve of linearized output: calibration run 8; tungsten wire; cold resistance 5·93 Ω, operating resistance 8·90 Ω. ○, calibration at beginning of particular run; □, calibration at end of same run.

	U_0	
W_0	33·2 ft s^{-1} ($R = 4{\cdot}14 \times 10^4$)	63·9 ft s^{-1} ($R = 7{\cdot}95 \times 10^4$)
0	Mean velocity measurements	Mean velocity and turbulence measurements
59·5 ft s^{-1}	Mean velocity and turbulence measurements	Mean velocity and turbulence measurements

TABLE 1. Summary of measured quantities and the conditions under which they are obtained.

Finally, the rotation speed was well above the critical frequency of the model of 200 rev/min estimated from the observed peak vibrations. At the working speed, vibrations were practically non-existent. Within the accuracy of our traversing mechanism (± 0·001 in.), the contact point was found to be the same for both dynamic and static conditions.

Measurements were performed in four different situations, summarized in table 1.† It is recalled that the rotation rate was always kept the same in all cases, but that mainstream velocity was varied instead. Static pressures were recorded on the tunnel walls and not on the model itself, for evident reasons.

---

† Tabulations of all of the data may be obtained by writing to the second author.

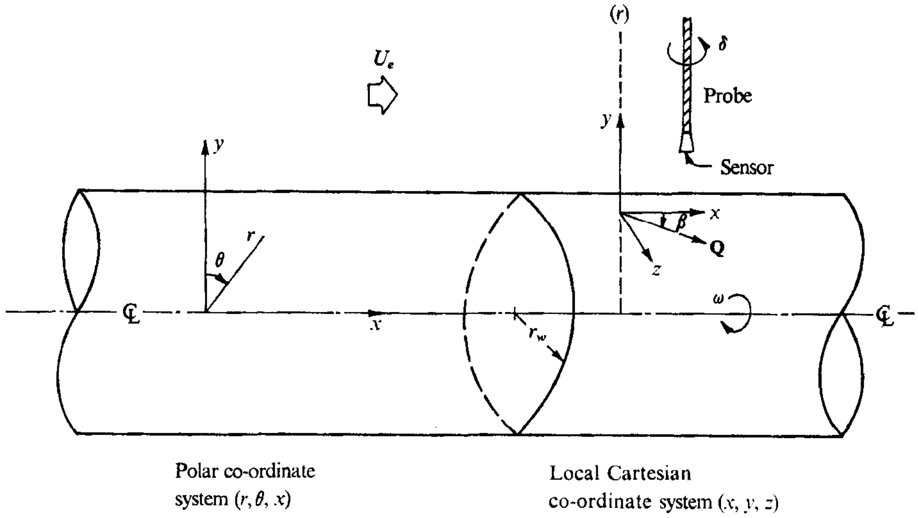

FIGURE 3. Co-ordinate systems. Q is local mean velocity vector.

3. Mean flow measurements

A hot-wire technique was developed for measurements of skewed velocity profiles. In the other cases when no rotation was present, a standard flattened head Pitot probe was used. The hot-wire probes were commercially made, and two types of sensors were used. The factory-mounted wires were first used; they were tungsten 0·00015 in. in diameter and 0·05 in. long with both ends copper plated. In other instances the broken sensors were replaced by soldering pre-etched tungsten wires, 0·0002 in. in diameter. A linearizer was used in conjunction with the constant-temperature anemometer. Calibration was performed using a small portable open return wind tunnel. A sample calibration curve is shown in figure 2.

For mean flow measurements, a straight hot-wire probe (sensor mounted perpendicular to the stem axis) was introduced and traversed along a radius of the cylinder as shown in figure 3. The probe was attached to a driving mechanism which rotated its stem very slowly ($\sim$ 1 degree s^{-1}) in both directions. The hot-wire signal was linearized, filtered and connected to the y input of an x, y plotter. The x input of the latter was fed with the voltage output of a potentiometer mechanically coupled to the driving device.

The mean value of a linearized hot-wire signal follows the law

$$\overline{e_L} = KQf(\phi), \tag{1}$$

where Q is the magnitude of the mean velocity vector, ϕ is the angle of attack and K is the linearizer calibration constant. The function $f(\phi)$ represents the directional properties of the sensor, and is normalized so that $f(0) = 1$. Referring to figure 4(a), which illustrates the plane of rotation of the wire, it is easy to show

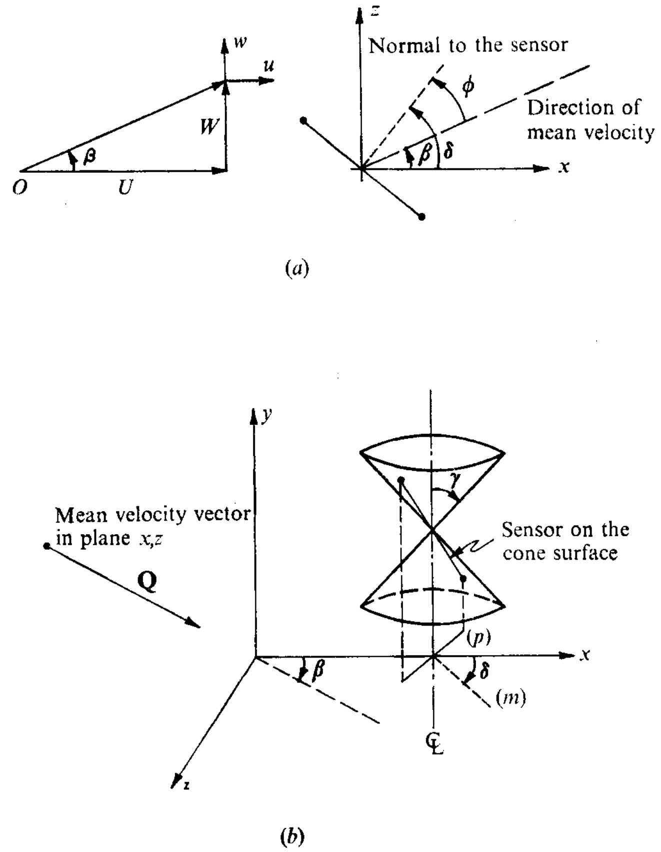

FIGURE 4. Co-ordinate systems. (*a*) For rotated straight-wire probe. Sensor in x, z plane. (*b*) For slanted-wire probe. (*p*) is projection of sensor in x, z plane. (*m*) is normal to line (*p*) in x, z plane.

that in the present case (1) can be rewritten as

$$\overline{e_L} = K(U^2 + W^2)^{\frac{1}{2}} f(\delta - \beta), \tag{2}$$

where δ is the relative angle of rotation and β the mean flow angle.

The experimental procedure was as follows. At a given height, the signal $\overline{e_L}$ was recorded against δ and the maximum value $(\overline{e_L})_{\max}$ was read on a digital voltmeter. Rotation was chosen to span approximately the range

$$-40^\circ < (\delta - \beta) < 40^\circ,$$

and recording was always performed in the same direction, to minimize the backlash errors. Figure 5 shows a typical series of those traces.

To reduce mean flow data, it was not necessary to specify completely the function $f(\phi)$. It is required only that $f(\phi)$ be symmetric with respect to its argument and pass through a maximum at $\phi = 0$. Therefore, both the direction β and magnitude Q of the local mean velocity vector could be determined simultaneously from the calculation of the point of symmetry δ_s, of each trace,

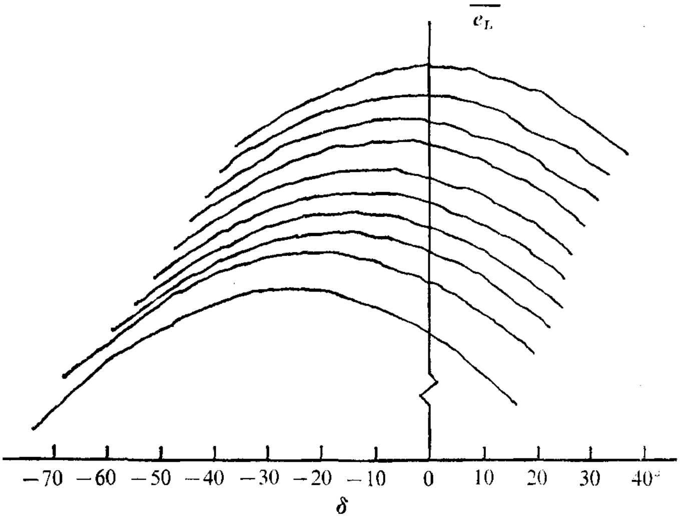

FIGURE 5. Sample traces for mean velocity measurements.

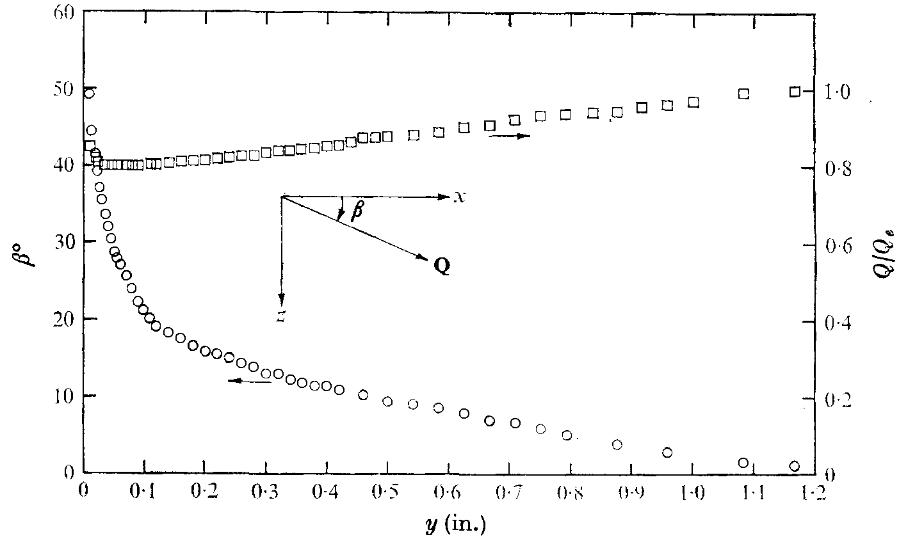

FIGURE 6. Sample profiles of magnitude and direction of mean velocity. $R = 4{\cdot}14 \times 10^{-4}$ is the Reynolds number based on the mainstream velocity and the radius of the cylinder. $\Omega = W_0/U_0 = 1{\cdot}8$ is the rotation rate. $\mathbf{Q}$ is local mean flow velocity vector. Station 8. ○, β; □, Q/Q_e.

and from the reading of its maximum value, according to

$$\delta_s - \beta = 0, \quad (\overline{e_L})_{\max} = K(U^2 + W^2)^{\frac{1}{2}}. \qquad (3), (4)$$

Thus, measurements of δ_s and $(\overline{e_L})_{\max}$ were sufficient to specify completely the skewed velocity profiles. A reference angle for δ was obtained by setting $\beta = 0$ when the sensor was located well outside the boundary layer and the rotating cylinder was turned off. (The mainstream direction is the relevant reference angle of our flow field.) As a test of consistency, mean velocity profiles measured with this technique were compared with those obtained with a Pitot probe in the case of no rotation. The agreement was better than 1 % of the local value, and fluctuations in the measured flow angle were smaller than 0·5°. Sample profiles for β and Q are shown in figure 6.

4. Turbulence measurements

For measurements of turbulent velocity moments, we selected a hot-wire method which is a modification of a technique proposed by Fujita & Kovasznay (1968). A block diagram of the anemometer system is shown in figure 7. The experimental procedure was divided into two sets of measurements. First, a straight-wire probe (same definition as in §3) was introduced and rotated as described in §3. In this case, both the mean and mean-square value of the linearized signal were recorded against the angle δ of rotation by means of x, y plotters. Second, a 45° slanted-wire probe (the sensor makes a 45° angle with the stem axis) was similarly introduced and rotated. The same variables were recorded in the same manner. The latter probe was positioned in such a way as to keep the longest prong always behind (or parallel to) the shortest one during rotation. Figures 4 (*a*) and (*b*) illustrate the principal features for both cases, respectively.

In figures 8 and 9, a sample record for the mean and mean-square value are shown (straight-wire probe). Recordings were performed in both directions of rotation. This was thought necessary to account for differences in hysteresis due to the different time constants of the low pass filter and the RMS meter. The true signal was interpreted by drawing an average curve between both traces. However, to reduce experimentation time, the two time constants were chosen approximately equal, and, assuming comparable hysteresis, recording in only one direction was required. Results obtained by the latter method did not differ practically from those obtained by the former.

It is evident in figures 8 and 9 that traces for the mean-square value have a higher noise level. This could have been eliminated by choosing a larger integration constant for the RMS meter. However, since rotation speed had to be kept within practical limits, there would have resulted a more widespread hysteresis, which would have caused serious interpretation problems. Therefore, the choice of a particular integration constant was a compromise between noise level and hysteresis. In all cases reported here, it was set at 3 s.

In the two sets of measurements, the sensor was rotated about the mean flow angle β. However, it must be stressed that accurate preliminary knowledge of β is not necessary; a rough estimate is quite sufficient. At each measuring point, the true angle β can be computed from the point of symmetry of the mean value record according to the technique described in §3. It is a built-in feature, so no critical alignment is required.

Data reduction was performed as follows. The derivation of the pertinent equations for the following analysis can be found in Bissonnette (1970). They are recalled here, and specialized for the use of a linearizer with calibration constant K. The reader is referred to figures 4 (*a*) and (*b*) for an illustrated definition of the variables. The working equations are summarized below.

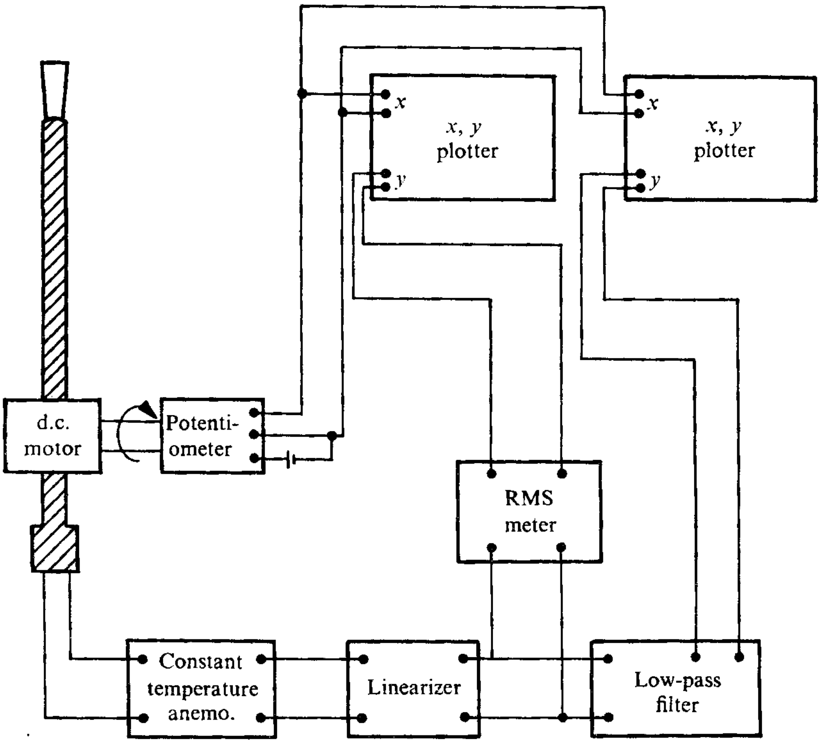

FIGURE 7. Block diagram of hot-wire anemometer system.

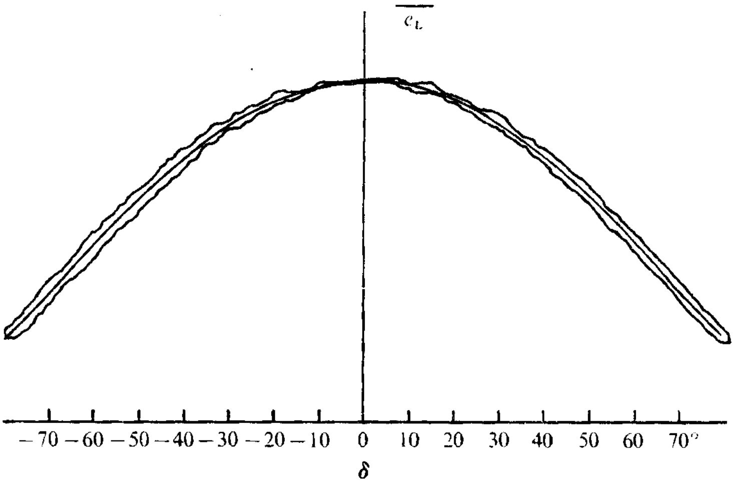

FIGURE 8. Sample traces of linearized mean voltage output.

Straight-wire probe

$$\phi = \delta - \beta, \tag{5}$$

$$\overline{e_L} = K(U^2 + W^2)^{\frac{1}{2}} f(\phi), \tag{6}$$

$$\overline{e_L'^2} = K^2\{f^2(\phi)\overline{u^2}^* - 2f(\phi)f'(\phi)\overline{uw}^* + f'^2(\phi)\overline{w^2}^*\}. \tag{7}$$

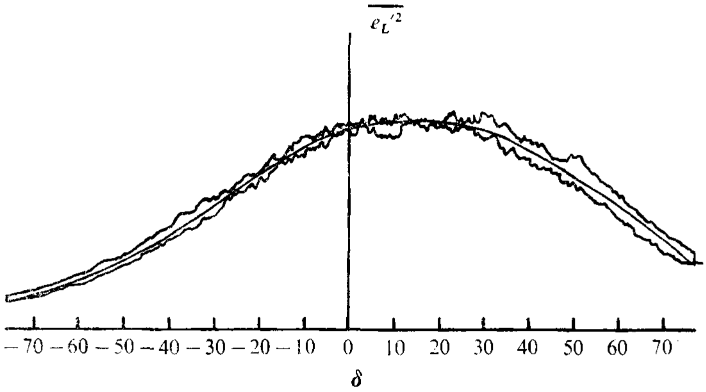

FIGURE 9. Sample traces of linearized mean-square voltage output.

Slanted-wire probe

$$\sin\phi = \sin\gamma\sin(\delta-\beta), \tag{8}$$

$$\overline{e_L} = K(U^2+W^2)^{\frac{1}{2}}f(\phi), \tag{9}$$

$$\begin{aligned}\overline{e_L'^2} = K^2\bigg\{&f^2(\phi)\,\overline{u^2}^* + \frac{\cos^2\gamma}{\cos^2\phi}f'^2(\phi)\,\overline{v^2}^* + \frac{\sin^2\gamma}{\cos^2\phi}\cos^2(\delta-\beta)f'^2(\phi)\,\overline{w^2}^*\\ &-2\frac{\cos\gamma}{\cos\phi}f(\phi)f'(\phi)\,\overline{uv}^* + 2\frac{\sin\gamma\cos\gamma}{\cos^2\phi}\cos(\delta-\beta)f'^2(\phi)\,\overline{vw}^*\\ &-2\frac{\sin\gamma}{\cos\phi}\cos(\delta-\beta)f(\phi)f'(\phi)\,\overline{uw}^*\bigg\}.\end{aligned} \tag{10}$$

The turbulent velocity moments with a superscript * are defined in a frame of reference aligned with local mean velocity vector. The moments in the frame of reference fixed to the axis of the cylinder are thus given by

$$\begin{aligned}\overline{u^2} &= \overline{u^2}^*\cos^2\beta - 2\overline{uw}^*\sin\beta\cos\beta + \overline{w^2}^*\sin^2\beta,\\ \overline{v^2} &= \overline{v^2}^*,\\ \overline{w^2} &= \overline{u^2}^*\sin^2\beta + 2\overline{uw}^*\sin\beta\cos\beta + \overline{w^2}^*\cos^2\beta,\\ \overline{uv} &= \overline{uv}^*\cos\beta - \overline{vw}^*\sin\beta,\\ \overline{vw} &= \overline{uv}^*\sin\beta + \overline{vw}^*\cos\beta,\\ \overline{uw} &= (\overline{u^2}^* - \overline{w^2}^*)\sin\beta\cos\beta + \overline{uw}^*(\cos^2\beta - \sin^2\beta).\end{aligned}$$

The angle of rotation δ is obtained from the calibrated x co-ordinate of each plot, and the flow angle β is computed as described earlier. The angle ϕ satisfies (5) or (8), depending on which case is considered. Hence, the function $f(\phi)$ can be experimentally evaluated from the mean voltage record, viz.

$$f(\phi) = \overline{e_L}(\phi)/\overline{e_L}(0).$$

However, since (7) and (10) involve derivatives of $f(\phi)$ the experimental data were fitted to a proposed functional form. The particular expression selected here was that suggested by Champagne, Sleicher & Wehrman (1967), i.e.

$$f^2(\phi) = \cos^2\phi + k^2\sin^2\phi. \tag{11}$$

The constant k was determined for each run, independently of any prior calibration. Thus, in this respect, the method can be said to be self-calibrating. In each case, k was computed as a mean value over all data points, i.e.

$$k^2 = \frac{1}{N}\sum_{i=1}^{N}\left\{\frac{\bar{e}_L^2(\phi_i)/\bar{e}_L^2(0) - \cos^2\phi_i}{\sin^2\phi_i}\right\}.$$

A typical value for k was 0·2. This scheme appears more accurate, inasmuch as it makes use of all available data points to compute local derivatives.

With the function $f(\phi)$ at hand, components $\overline{u^2}^*$, $\overline{w^2}^*$ and $\overline{uw}^*$ were obtained by least-square fitting (7) to the experimental record of $\overline{e_L'^2}$ (straight-wire probe). Substituting these results in (10), the remaining components $\overline{v^2}^*$, $\overline{uv}^*$ and $\overline{vw}^*$ were computed by a similar technique, using the $\overline{e_L'^2}$ record of the slanted-wire probe. In principle, (10) should be sufficient to determine all six components $\overline{u_i u_j}$, but in practice the accuracy of such a scheme was found to be inconsistent. The recordings were simply not accurate enough, and the limited range of ϕ imposed by the geometry was too short to permit the determination of six independent numbers from a single trace.

In view of the three-dimensionality of the flow under investigation, this rotating-wire method was preferred to the more classical X-probe technique. The latter requires a precise knowledge of the local mean flow direction for accurate positioning of the probe. Failing to do so would result in significant errors. As shown in the preceding paragraphs, this difficulty disappears, because the wire is allowed to rotate. Initially, rotation of an X-probe was considered, but it soon became evident that a single wire was not only sufficient, but also desirable to minimize the prong interference effects. Again, since a single wire was used, the matching of two slightly different sensors was not necessary. Furthermore, the method is so designed that no prior angular calibration was required: it was built-in by the determination of a new k at each point. One drawback, however, was the longer measuring time involved, which in its turn involved a more critical demand for stability of both the flow field and the electronic equipment.

The reader is reminded that, contrary to ordinary practice and because of the need for rotation, the probes were introduced with their prongs perpendicular to the mean flow. (In view of the relatively small thickness of the layers considered in this experiment, more elaborate probe configurations appeared very difficult to realize. Some attempts were made in this direction, but no appreciable advantages were realized.) Of course, the sensors were calibrated in the same configuration, and it is interesting to note that the measured constant k of (11) was found to approximate very well to the value predicted by Champagne *et al.* (1967) for the types of sensors used. This indicates that interference effects were not too critical.

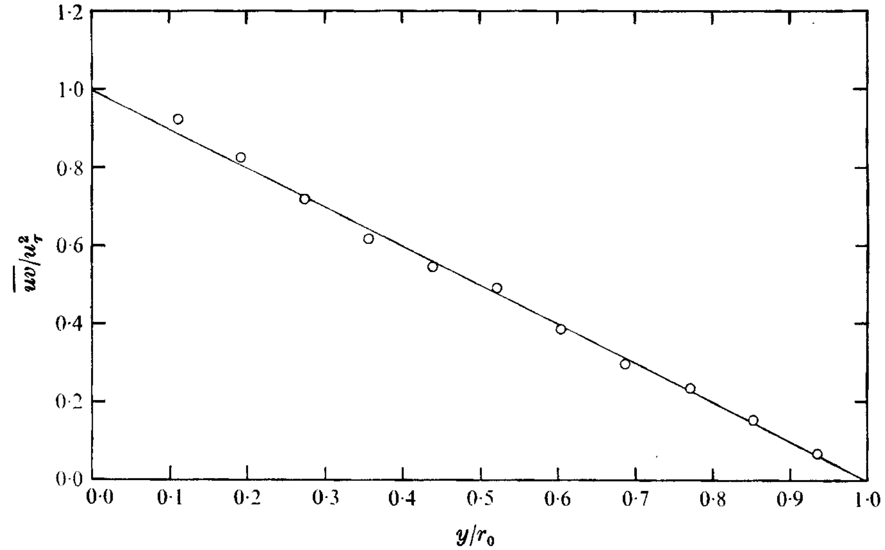

FIGURE 10. Comparison of theoretical (——) with measured (○) distribution of the turbulent stress $\overline{uv}$ in pipe flow. $R_D = 1{\cdot}7 \times 10^5$ is Reynolds number based on diameter of pipe. r_0, radius of pipe.

5. Evaluation of the experimental technique in pipe flow

Since most measurements reported in this article were obtained by techniques not previously used, it is worthwhile to evaluate the consistency and reliability of the data. First, a series of measurements was made in a fully developed pipe flow. Second, the no-rotation boundary-layer data were tested against classical two-dimensional results. Finally, consistency between mean flow and turbulence measurements was analysed. The fully developed pipe flow experiment is discussed here.

The apparatus consisted of two 18 ft long, 6 in. I.D. aluminium pipes. The air entered through a nozzle-diffuser combination, and was expelled at the other end by an axial flow fan driven by a variable speed d.c. motor. The axial pressure gradient was found to be linear over a distance of approximately 18–20 diameters upstream of the working section. From the theory of fully developed pipe flow, the friction velocity u_τ is given by

$$u_\tau^2 = -\frac{r_0}{2}\frac{1}{\rho}\frac{dP}{dx}, \qquad (12a)$$

and the Reynolds stress, except very close to the wall, is

$$\overline{uv} = u_\tau^2 r/r_0. \qquad (12b)$$

r_0 is the radius of the pipe and P is the static pressure.

In figure 10, our measurements for $\overline{uv}$ and u_τ^2 from (12a) are compared with (12b). The agreement is very good, better than 2 or 3%. As for the energy components, our data were compared with those of several investigators. The results

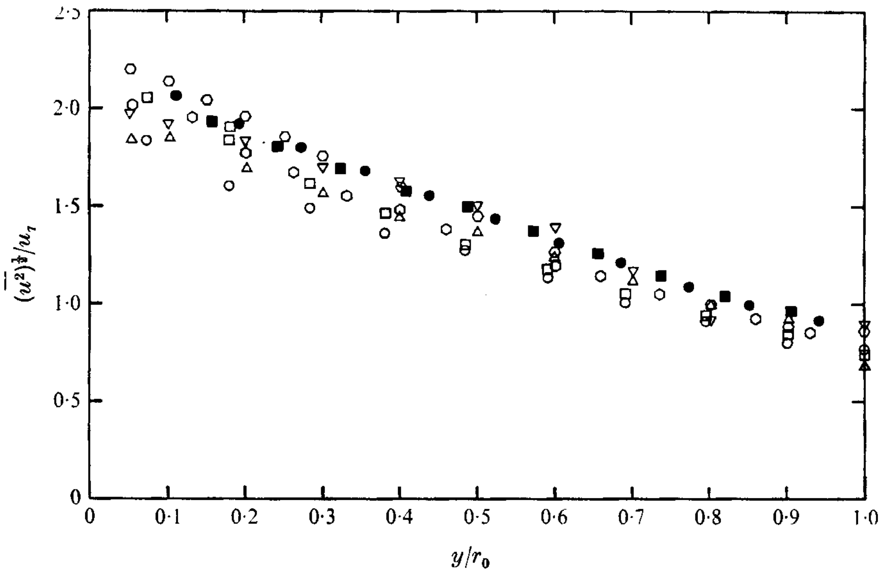

FIGURE 11. Distribution of $\overline{(u^2)}^{\frac{1}{2}}$ in pipe flow. R_D based on diameter of pipe. r_0, radius of pipe.

	Laufer (1953)		Sandborn (1955)		Patel (1963, 1968)		Authors	
$R_D \times 10^{-5}$	0·5	5·0	1·0	2·0	2·74	1·93	1·7	1·7
Data	○	□	▽	△	⬡	⬡	■	●

for $\overline{u^2}$ are illustrated in figure 11. It is shown that our measured values fall well within the scatter between the different sets of data, and similar agreement was also found for $\overline{v^2}$ and $\overline{w^2}$. Finally, the stress components $\overline{vw}$ and $\overline{uw}$, theoretically zero, were measured to be less than 5 % of the local $\overline{u^2}$, and were more or less randomly distributed.

Therefore, these results suggest that, under similar conditions, our anemometer technique permits the determination of the $\overline{u_i u_j}$'s to an accuracy better than 5 % of the local turbulent energy per unit mass. In §7 this statement is reviewed and slightly modified, on account of the special geometry of the present experiment.

6. Two-dimensional axisymmetric turbulent boundary layer

Before entering the subject of three-dimensional flow, it is important to verify how the unskewed layer (cylinder at rest) compares with classical two-dimensional results.

A first well-known property of two-dimensional layers is the law of the wall. As demonstrated by Richmond (1957), this must be slightly corrected to account for transverse curvature effects. Thus, for axisymmetric two-dimensional turbulent boundary layers,

$$U/u_\tau = f^+(u_\tau \bar{y}/\nu), \tag{13}$$

where

$$\bar{y} = y + y^2/2r_w, \tag{14}$$

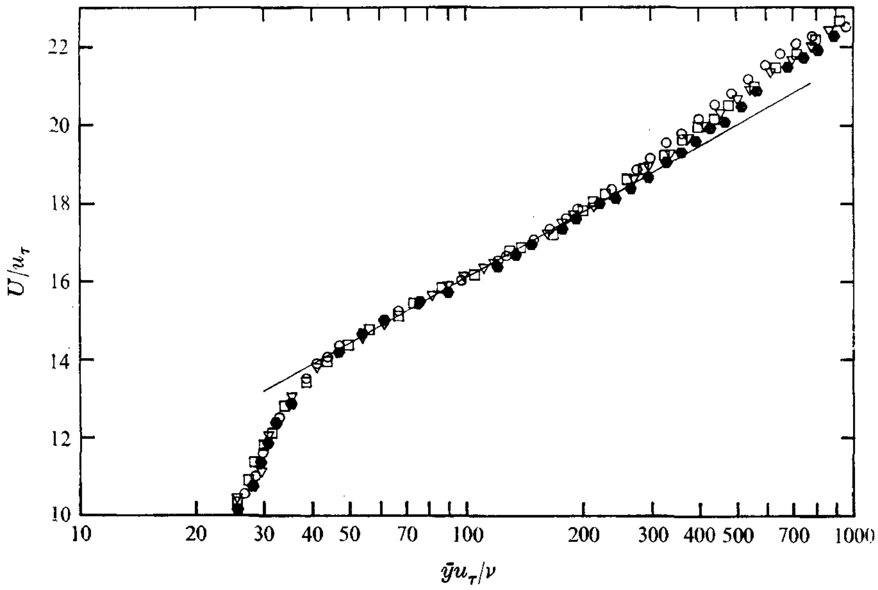

FIGURE 12. Law of the wall for unskewed (no rotation) boundary layer. $R = 7{\cdot}95 \times 10^4$, $\Omega = 0{\cdot}0$. Stations; □, 8; ●, 6; ▽, 4; ○, 1. ——, $U/u_\tau = 5{\cdot}6 \log_{10} \bar{y}\, u_\tau/\nu + 4{\cdot}9$.

and u_τ is the friction velocity. f^+ is the universal function usually associated with flat-plate boundary layers, and it is asymptotically logarithmic outside the sublayer region. The data for one Reynolds number case are plotted in figure 12. Agreement with the logarithmic portion of the law of the wall (in the proposed axisymmetric form) is very well shown. However, we note that the measured velocities are too low as $y \to 0$. This behaviour is difficult to understand, since errors very near the wall are common enough, but generally tend to be in the opposite direction.

A second property of two-dimensional layers is the velocity-defect law. This law is not as universal as the law of the wall, inasmuch as it depends on outer boundary conditions, especially pressure gradients. However, Clauser (1954) showed that there exists a similarity parameter

$$\beta_c = \frac{\delta^*}{\tau_w}\frac{dP}{dx},$$

which, if held constant, led to similar velocity-defect profiles. δ^* is the momentum thickness and τ_w the wall shear stress. In the present case, $\beta_c \simeq -0{\cdot}06$; since this is small, variations in β_c should not be significant. In figure 13 it is shown that our data for velocity defect do collapse on one curve.

An important feature of these inner (law of the wall) and outer (defect law) functions is the matching relation, which in this case is semi-logarithmic, provided that there exists an overlap region where both laws are valid. We have already seen that the outer asymptote of the law of the wall was given by

$$\frac{U}{u_\tau} = 5{\cdot}6 \log_{10} \frac{u_\tau}{\nu} \bar{y} + 4{\cdot}9. \qquad (15a)$$

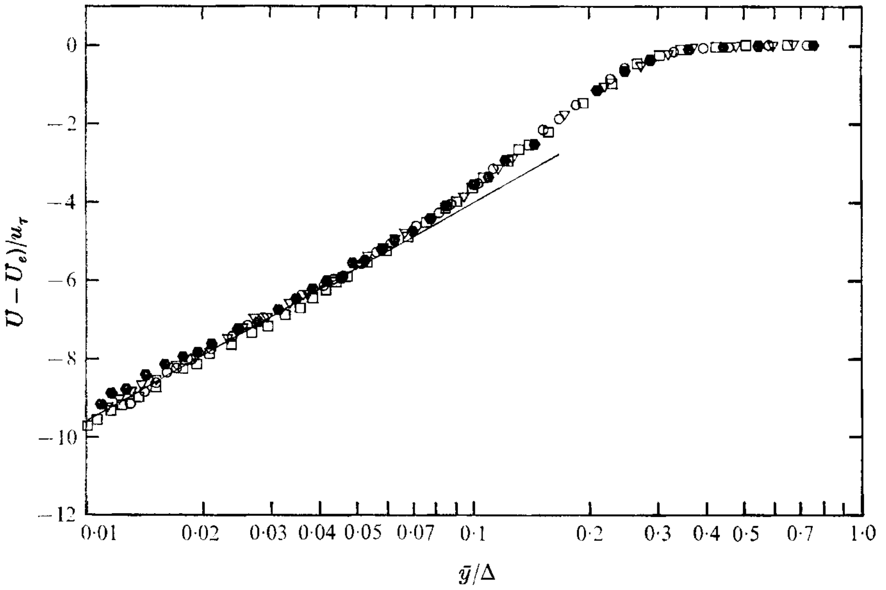

FIGURE 13. Velocity-defect law for unskewed (no rotation) boundary layer. R, Ω and symbols as in figure 12. ——, $(U_e-U)/u_\tau = -5{\cdot}6\log_{10}(\bar{y}/\Delta)-1{\cdot}6$.

Assuming the existence of a defect profile, the inner asymptote must be

$$\frac{U_e-U}{u_\tau} = -5{\cdot}6\log_{10}\frac{\bar{y}}{\Delta}+A(\beta_c). \qquad (15b)$$

In figure 13 we find that $A = -1{\cdot}6$. However, according to computations of Mellor & Gibson (1966), which were in agreement with flat-plate data, the equilibrium value of A corresponding to our β_c should be $-0{\cdot}8$. Therefore, the A obtained in figure 13 is too small. A similar situation is also evident in the work of Yu (1958), and may be attributed to the effect of transverse curvature (Richmond 1957; Probstein & Elliot 1956). Indeed, the axisymmetric mean momentum equation contains an additional stress term in comparison with the flat-plate equation. This term arises directly because of the curvature and is similar in effect to a favourable pressure gradient. In Mellor & Gibson (1966) and Herring & Norbury (1967), it is shown that a favourable pressure gradient means a smaller A, so that the present result is not unexpected.

In summary, our unskewed layer constitutes a well-behaved flow, and some interesting consequences of transverse curvature are confirmed. These observations, together with those of § 2–5, add to our confidence in both the general flow field and the experimental method.

7. The three-dimensional axisymmetric data

The development of the axial and circumferential velocity profiles is shown in figures 14 and 15. To save space, we shall present the complete data for only one rotation rate, although three-dimensional measurements were performed in two

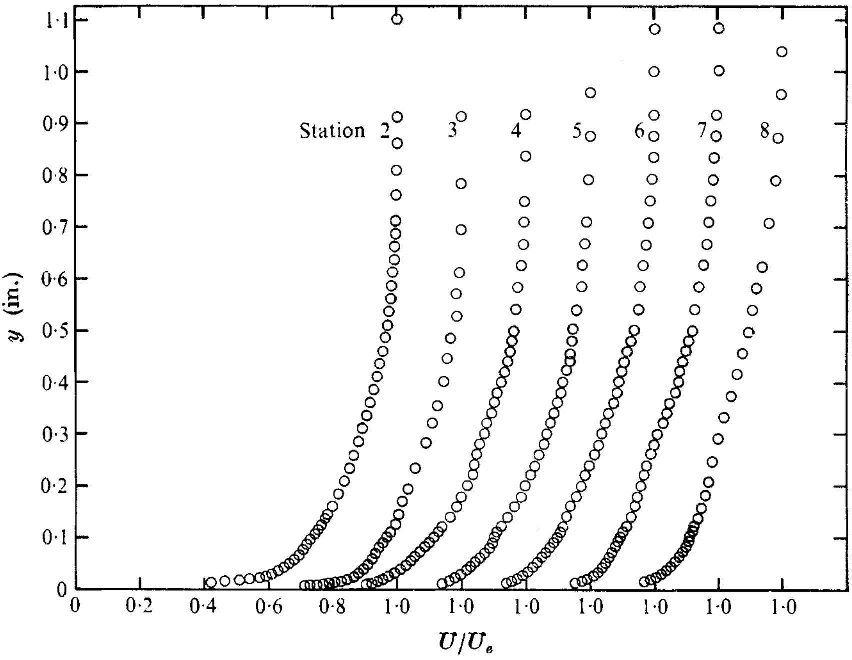

FIGURE 14. Experimental distribution of axial component of velocity. $R = 7{\cdot}95 \times 10^4$, $\Omega = 0{\cdot}936$.

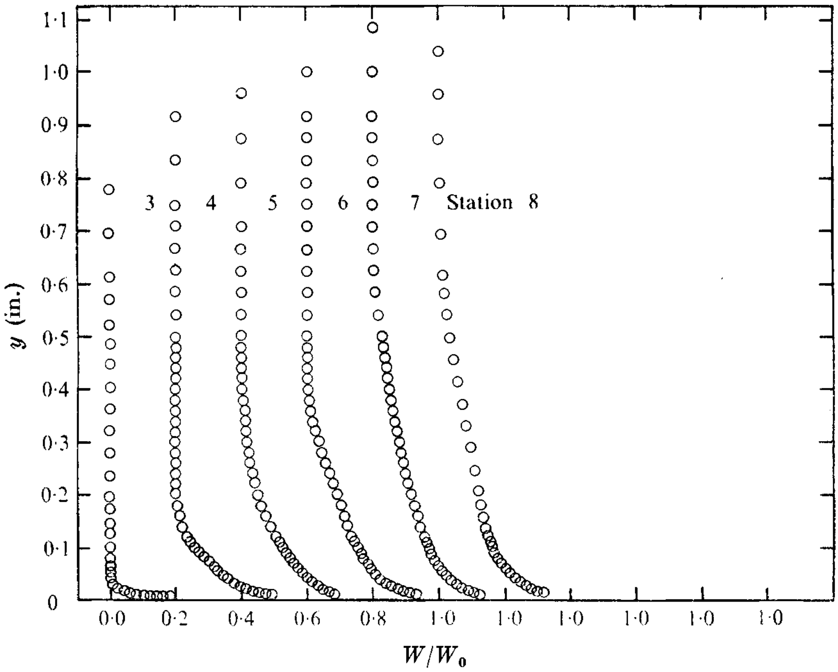

FIGURE 15. Experimental distribution of transverse component of velocity. $R = 7{\cdot}95 \times 10^4$, $\Omega = 0{\cdot}936$.

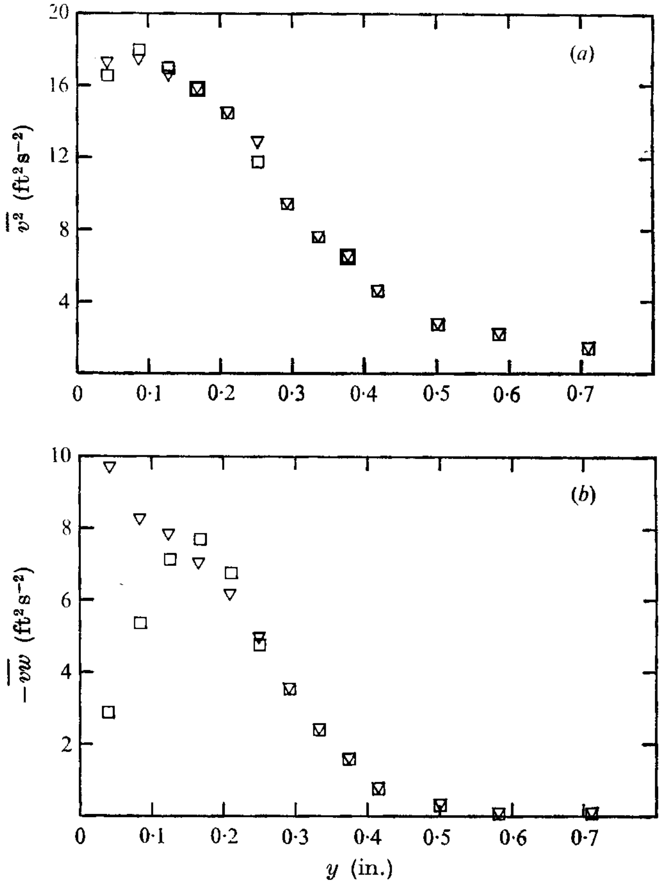

FIGURE 16. Comparison of measured velocity moments, using two methods of interpretation: □, direct method (mean flow angle β evaluated at centre point of slanted wire); ▽, corrected method, using measured profile of β (coefficients in (10) are integrated over wire length to account for mean flow skewness).

cases, as shown in table 1. The rotation rate is defined as the ratio W_0/U_0, where W_0 is the surface velocity of the cylinder, and U_0 the mainstream velocity averaged over all x stations. However, in the following discussions we shall frequently cite partial data from both sets.

Although the pipe flow measurements were gratifying, it became evident that there were errors in $\overline{uv}$ and $\overline{vw}$ when the technique was applied to the rotating cylinder experiment. Errors were introduced because of the small scale size and the large degree of skewness in the mean flow near the cylinder surface. Since the sensor makes a 45° angle with the wall, this causes the angle β, and hence the angle of attack ϕ, to vary considerably over the wire length. A rapid inspection of (8)–(10) shows that under these circumstances the interpretation of the record $\overline{e_L'^2}$ in the case of the slanted-wire probe becomes rather unreliable. Moreover, it was noticed that prong interference effects were more evident in that region: this was indicated by the measured constant k of (11), which was found to be smaller in those cases; k^2 was even negative in some instances. A correction

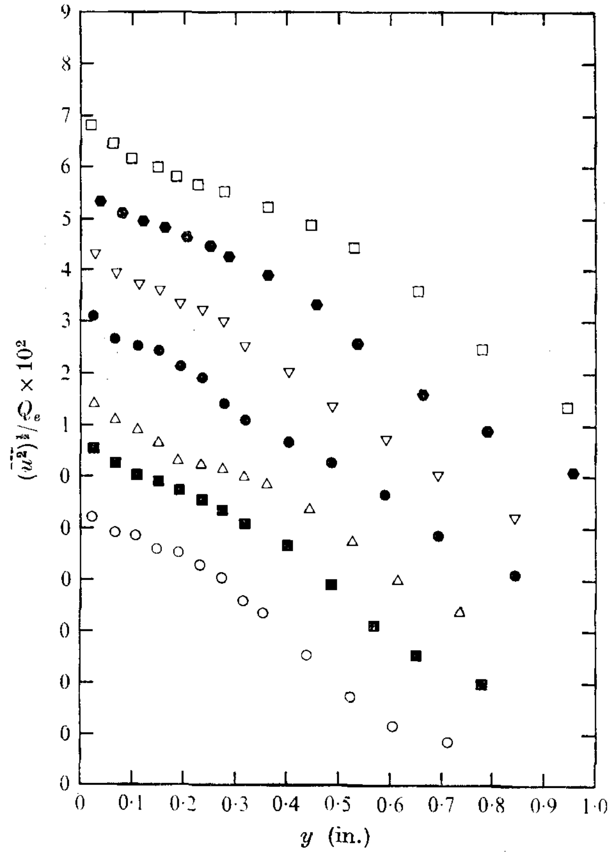

Figure 17. Experimental distribution of $(\overline{u^2})^{\frac{1}{2}}$. $R = 7{\cdot}95\times 10^4$, $\Omega = 0{\cdot}936$.

Station	1	3	4	5	6	7	8
	○	■	△	●	▽	⬢	□

was introduced by integrating the coefficients of (10) over the length of the wire, using the measured distribution of β (Bissonnette 1970).

A typical comparison between corrected values and those obtained simply by evaluating β at the centre point of the wire is presented in figure 16. It is shown that relatively large differences, especially in $\overline{vw}$, are found near the wall. The differences in $\overline{v^2}$ are much less significant.

The data presented in this paper were obtained by the corrected method of interpretation, but owing to the size of the corrections, there remain some questions concerning the accuracy of $\overline{uv}$ and $\overline{vw}$ in the near wall region, which, from information similar to that illustrated in figure 16, was defined empirically in the present case as $y/l_s < 2$, where l_s is the wire length. As for the other components $\overline{u^2}$, $\overline{w^2}$ and $\overline{uw}$, the problem does not arise, since they were obtained with a straight-wire probe, in which case the sensor is rotated in a plane parallel to the wall. It would seem that a smaller wire length should have minimized the gradient effects. This was actually tried, but, with the particular probe configuration used in this experiment, the prong interference effects obscured any improvement.

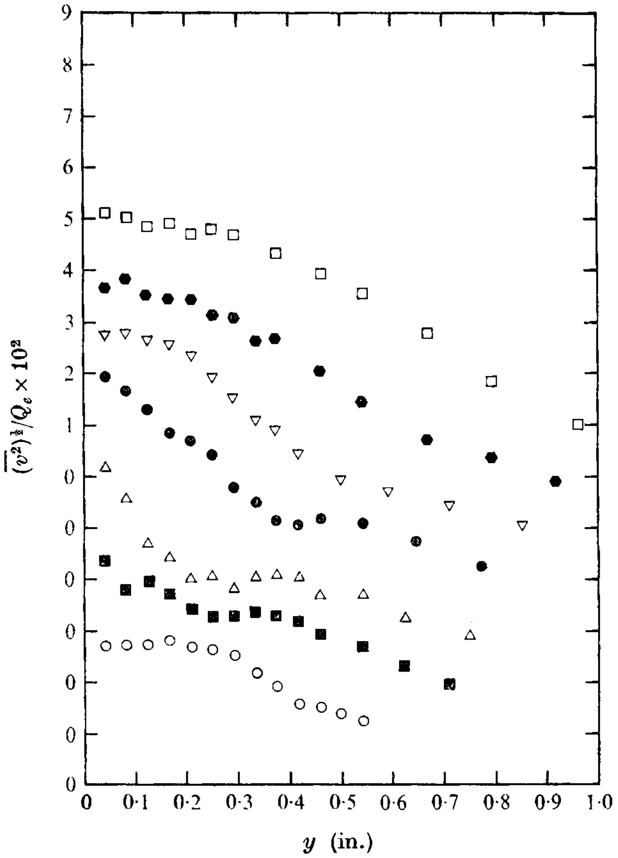

FIGURE 18. Experimental distribution of $(\overline{v^2})^{\frac{1}{2}}$. R, Ω, symbols as in figure 17.

8. Integration of mean momentum equations

Although the corrected $\overline{uv}$ and $\overline{vw}$ data appear reasonable, the corrections near the wall were rather large and further corroboration seemed desirable. Luckily, these quantities can be obtained, in principle, from the mean momentum equations. This procedure is hazardous in the case of plane flows of finite aspect ratio, owing to the ubiquitous presence of secondary flows. However, with the present axisymmetric geometry this problem does not seem to be serious. In this regard, we should mention that the assumption of axisymmetry was verified experimentally from measurements of mean velocity profiles in different meridional planes. The agreement was better than 1 % of the local value.

Assuming axisymmetry, the boundary-layer approximation to the equations of mean motion can be written as

$$\frac{\partial}{\partial x}(rU)+\frac{\partial}{\partial r}(rV) = 0, \tag{16}$$

$$U\frac{\partial U}{\partial x}+V\frac{\partial U}{\partial r} = -\frac{1}{\rho}\frac{\partial P}{\partial x}+\frac{1}{r}\frac{\partial}{\partial r}\left(r\frac{\tau_x}{\rho}\right), \tag{17}$$

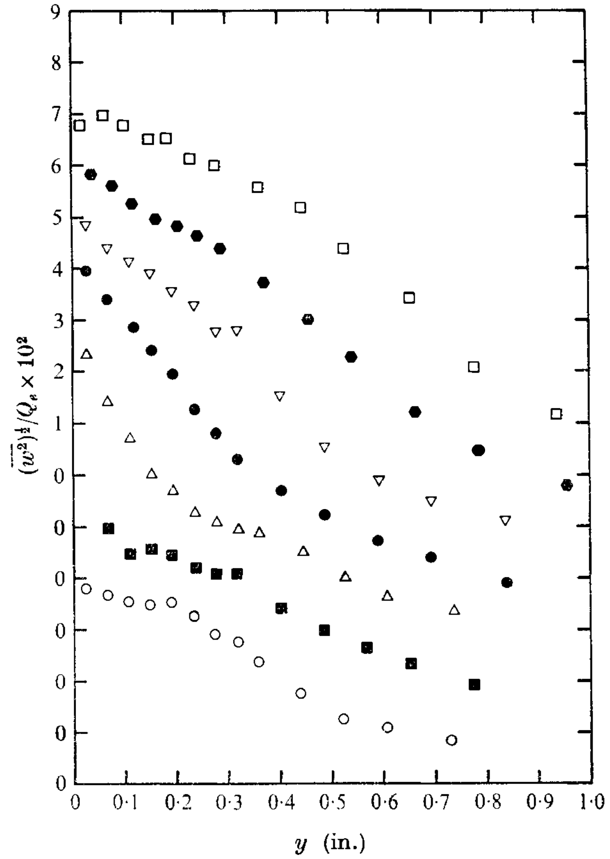

FIGURE 19. Experimental distribution of $(\overline{w^2})^{\frac{1}{2}}$. R, Ω, symbols as in figure 17.

$$U\frac{\partial W}{\partial x}+\frac{V}{r}\frac{\partial}{\partial r}(rW)=\frac{1}{r^2}\frac{\partial}{\partial r}\left(r^2\frac{\tau_z}{\rho}\right), \tag{18}$$

$$\frac{1}{\rho}\frac{\partial P}{\partial r}=\frac{W^2}{r}+\frac{\overline{w^2}}{r}-\frac{1}{r}\frac{\partial}{\partial r}(r\overline{v^2}), \tag{19}$$

where

$$\frac{1}{\rho}\tau_x=-\overline{uv}+\nu\frac{\partial U}{\partial r}, \tag{20a}$$

$$\frac{1}{\rho}\tau_z=-\overline{vw}+\nu\left(\frac{\partial W}{\partial r}-\frac{W}{r}\right). \tag{20b}$$

After substitution of the measured U and W into (16)–(19), the shear stress distributions τ_x and τ_z were computed numerically. The boundary conditions were that τ_x and τ_z must vanish at the edge of the layer. The computation is straightforward in principle, but in practice it led to some difficulties, since it involved numerical differentiation of measured quantities. Thus $\partial U/\partial x$ and $\partial W/\partial x$, in particular, are numerically determined by small differences of larger numbers. After considerable trial, the simplest method of a best straight-line fit to the data

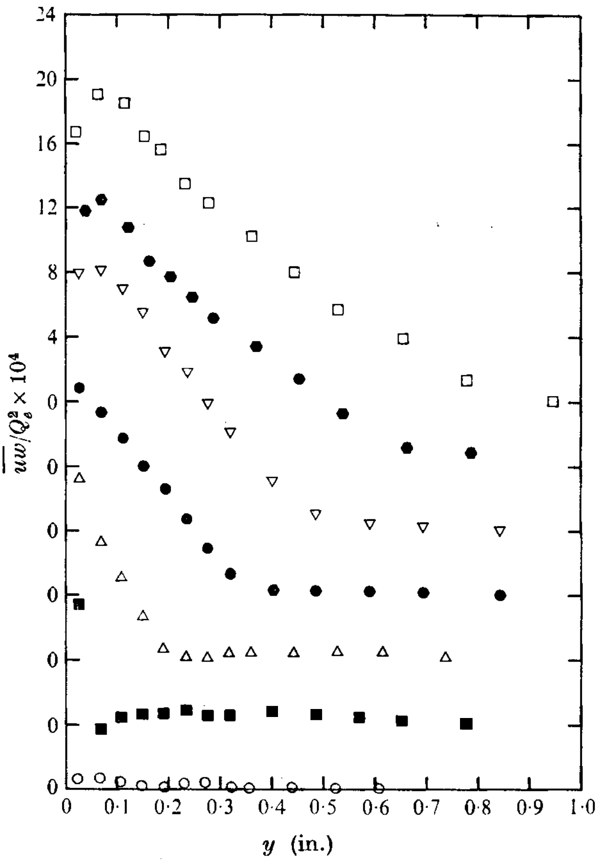

FIGURE 20. Experimental distribution of $\overline{uw}$. R, Ω, symbols as in figure 17.

at three adjacent stations was selected. Along with the data, the results of this analysis are shown in figures 21 and 22.

As might have been expected, the procedure described above smooths in the y direction while introducing fluctuations in the x direction. Nevertheless, the overall conclusion is that the hot-wire measurements and the finite wire length correction are corroborated, and there is not likely to be an appreciable systematic error in the measurements. Note, therefore, that the detailed variations in the data are likely to be real, except near the wall. However, the data of station 3, and possibly 4, should be excluded from this endorsement, because the x variations of the Reynolds stresses have been neglected in the momentum equations.

In table 2 we list the values of τ_{x_w} and τ_{z_w} (obtained by extrapolating the data to the wall, using the slopes of the calculated curves as a guide: in this process one or two data points near the wall were discarded, if they were deemed particularly inconsistent) along with the experimental momentum and displacement thicknesses.

(*a*) $R = 7.95 \times 10^4$

	$\Omega = 0{\cdot}0$			$\Omega = 0{\cdot}936$					
x (in.)	δ_x^* (in.)	θ_x (in.)	C_f	δ_x^* (in.)	δ_z^* (in.)	θ_x (in.)	θ_{xz} (in.)	C_{f_x}	C_{f_z}
−6	0·089	0·064	0·0039	0·089	0	0·064	0	0·0021	0
−1	0·101	0·070	0·0038	0·101	0	0·070	0	0·0020	0
1	0·107	0·074	0·0037	0·088	0·008	0·064	0·001	—	—
4	0·109	0·079	0·0037	0·105	0·022	0·074	0·010	—	—
8	0·113	0·082	0·0037	0·113	0·040	0·082	0·023	0·0027	0·0025
13	0·127	0·093	0·0036	0·132	0·052	0·094	0·032	0·0028	0·0026
18	0·140	0·102	0·0035	0·145	0·072	0·108	0·050	0·0027	0·0023
23	0·148	0·107	0·0034	0·158	0·081	0·115	0·056	0·0026	0·0021

(*b*) $R = 4{\cdot}14 \times 10^4$

	$\Omega = 0{\cdot}0$			$\Omega = 1{\cdot}8$					
x (in.)	δ_x^* (in.)	θ_x (in.)	C_f	δ_x^* (in.)	δ_z^* (in.)	θ_x (in.)	θ_{xz} (in.)	C_{f_x}	C_{f_z}
−6	0·103	0·073	0·0045	0·103	0	0·073	0	0·0011	0
−1	0·121	0·085	0·0044	0·121	0	0·085	0	0·0011	0
1	0·125	0·088	0·0043	0·102	0·002	0·077	0·002	—	—
4	0·129	0·092	0·0043	0·121	0·018	0·088	0·018	—	—
8	0·131	0·095	0·0043	0·123	0·037	0·091	0·038	0·0018	0·0041
13	0·143	0·103	0·0041	0·161	0·058	0·118	0·058	0·0017	0·0037
18	0·150	0·108	0·0041	0·187	0·081	0·143	0·083	0·0017	0·0035
23	0·159	0·117	0·0040	0·193	0·101	0·153	0·100	0·0016	0·0031

TABLE 2. List of the experimentally measured thicknesses and skin friction coefficients.

$$\delta_x^* = \int_{r_w}^{\infty} \frac{r}{r_w}\left(1-\frac{U}{U_e}\right)dr, \quad \delta_z^* = \int_{r_w}^{\infty} \frac{r^2}{r_w^2}\frac{|W|}{W_0}\,dr, \quad \theta_x = \int_{r_w}^{\infty} \frac{r}{r_w}\frac{U}{U_e}\left(1-\frac{U}{U_e}\right)dr, \quad \theta_{xz} = \int_{r_w}^{\infty} \frac{r^2}{r_w^2}\frac{U}{U_e}\frac{|W|}{W_0}\,dr,$$

$$C_f = \tau_w/\tfrac{1}{2}\rho U_e^2, \quad C_{f_x} = \tau_{x_w}/\tfrac{1}{2}\rho Q_e^2 \quad (Q_e^2 = U_e^2 + W_0^2), \quad C_{f_z} = \tau_{z_w}/\tfrac{1}{2}\rho Q_e^2.$$

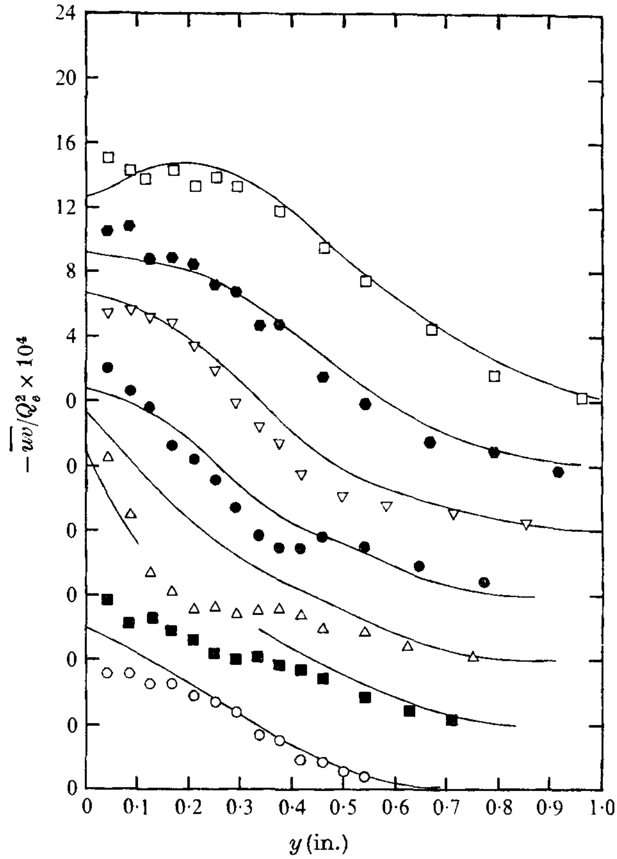

FIGURE 21. Experimental distribution of $\overline{uv}$, R, Ω, symbols as in figure 17. ——, total stress computed from integration of momentum equations.

9. Three-dimensional axisymmetric turbulent boundary layer

In the following discussion, emphasis is placed on proposed extensions of existing two-dimensional theories. In particular, we shall examine the validity of a scalar eddy viscosity model, and at the same time, investigate some aspects of Johnston's triangular model. We begin our analysis by plotting hodograph diagrams in figures 23 and 24. At every x station, the velocity vectors for each value of the co-ordinate y normal to the wall were drawn on a plane parallel to the wall, from a single origin. This technique was proposed by Johnston (1960). In the present case, we plot U against rW/r_w. The relevance of the geometric factor r/r_w will appear later, when we consider the defect layer.

These experimental curves suggest that we divide our analysis into two regions: one region near the wall, where the data can be approximated by a straight line passing through the origin, which in this experiment is $U = 0$ and $W = -W_0$, and an outer region which, after a transistory regime, evolves to a point where the data can be approximated by a line segment passing through the mainstream values $U = U_e$ and $W = 0$.

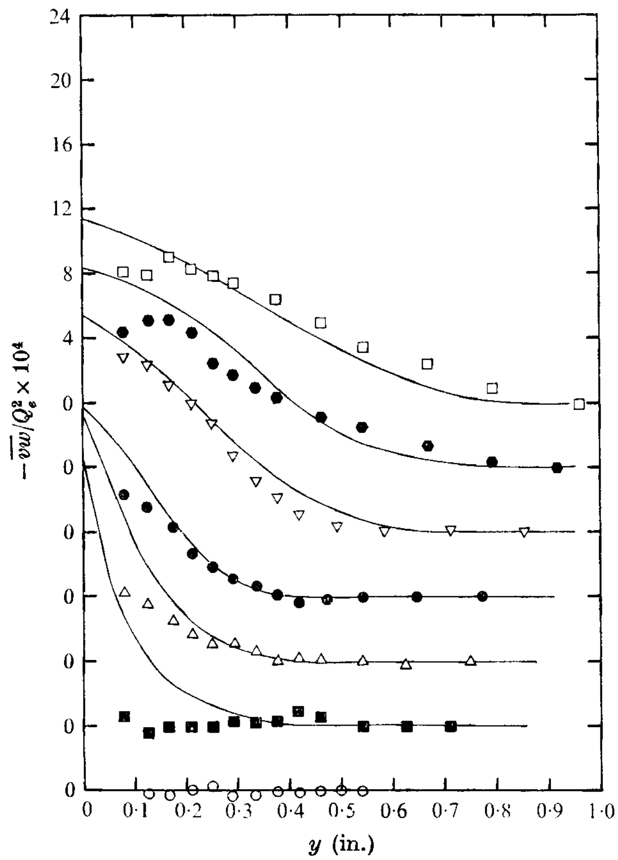

FIGURE 22. Experimental distribution of $\overline{vw}$. R, Ω, symbols as in figure 17; curve as in figure 21.

The behaviour of the data in the inner layer can be predicted from the equations of mean motion. In the wall region, a justified approximation consists of neglecting the acceleration terms. Hence, the mean momentum equations (17) and (18) become

$$\frac{r}{r_w}\left[-\overline{uv}+\nu\frac{\partial U}{\partial r}\right]=\frac{1}{\rho}\tau_{x_w}(x), \tag{21a}$$

$$\frac{r^2}{r_w^2}\left[-\overline{vw}+\nu\left(\frac{\partial W}{\partial r}-\frac{W}{r}\right)\right]=\frac{1}{\rho}\tau_{z_w}(x). \tag{21b}$$

In the limit $y \to 0$, the viscous contribution to the stresses is dominant, thus $(21a, b)$ can be written as

$$\left(\frac{\partial W}{\partial r}-\frac{W}{r}\right)\Big/\frac{\partial U}{\partial r}\sim\frac{r_w}{r}\frac{\tau_{z_w}}{\tau_{x_w}} \quad (y \to 0), \tag{22}$$

or, defining $$\tan\theta_w = \tau_{z_w}/\tau_{x_w},$$

$$W_0 + W \sim U\tan\theta_w(x) \quad (y \to 0). \tag{23}$$

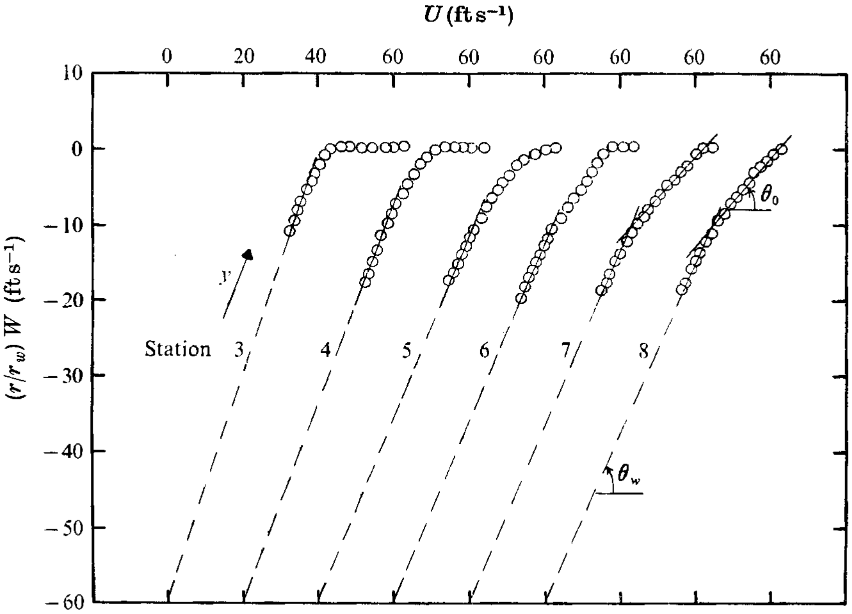

FIGURE 23. Hodograph diagrams of mean velocity vectors for $\Omega = 0{\cdot}936$, $R = 7{\cdot}95 \times 10^4$.

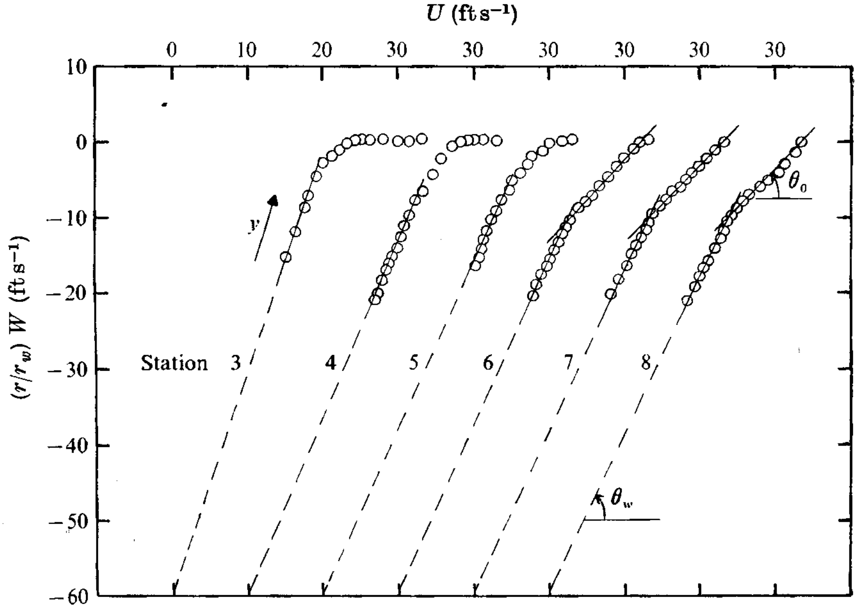

FIGURE 24. Hodograph diagrams of mean velocity vectors for $\Omega = 1{\cdot}8$, $R = 4{\cdot}14 \times 10^4$.

However, the requirement of negligible turbulent stresses, which was introduced to permit passage from (21 a, b) to (22), cannot be justified at the relatively large values of y for which (22) and (23) are still confirmed experimentally.

It is sufficient, in order to recover this experimental result, to make the hypothesis of a scalar turbulent or eddy viscosity, i.e.

$$-\overline{uv} = \nu_T \frac{\partial U}{\partial r}, \qquad -\overline{vw} = \nu_T \left(\frac{\partial W}{\partial r} - \frac{W}{r} \right). \qquad (24a, b)$$

Using (24 a, b) in (21 a, b), it follows that (22) and (23) are also valid at the larger values of y observed in figures 23 and 24. Although (24 a, b) do not constitute necessary conditions, the above analysis indicates that a scalar effective eddy viscosity is a plausible model in the law of the wall region.

We next turn our attention to the observed asymptotic behaviour of the polar diagrams in the outer region of the boundary layer. We shall show that this constitutes a solution of the equations of mean motion asymptotically valid at small velocity defects. To simplify matters, we first introduce the approximation†

$$\frac{\partial P}{\partial x} \simeq \frac{dP_e}{dx} = -\rho U_e \frac{dU_e}{dx}. \qquad (25)$$

Multiplying (17) by $\sin\theta$ and (18) by $-r\cos\theta/r_w$, where θ is assumed an arbitrary function of x, and adding, we obtain

$$U \sin\theta \frac{\partial U}{\partial x} - U \cos\theta \frac{\partial}{\partial x}\left(\frac{r}{r_w} W \right) - U_e \sin\theta \frac{dU_e}{dx}$$
$$+ V \frac{\partial}{\partial r}\left\{ U \sin\theta - \frac{r}{r_w} W \cos\theta \right\} = \frac{1}{r}\frac{\partial}{\partial r}\left\{ \frac{r}{\rho}\tau_x \sin\theta - \frac{r^2}{r_w}\frac{1}{\rho}\tau_z \cos\theta \right\}.$$

Adding and subtracting $U \sin\theta\, dU_e/dx$ and $U(U_e - U)(1/\cos\theta)\, d\theta/dx$ and rearranging, the above equation can be rewritten as

$$-U \sin\theta \frac{\partial}{\partial x}\left\{ (U_e - U) + \frac{r}{r_w}\frac{W}{\tan\theta} \right\} - \frac{U}{\cos\theta}\frac{d\theta}{dx}\left\{ (U_e - U) + \frac{r}{r_w}\frac{W}{\tan\theta} \right\}$$
$$- V \sin\theta \frac{\partial}{\partial r}\left\{ (U_e - U) + \frac{r}{r_w}\frac{W}{\tan\theta} \right\} + (U_e - U)\left\{ \frac{U_e}{\cos\theta}\frac{d\theta}{dx} - \sin\theta\frac{dU_e}{dx} \right\}$$
$$-(U_e - U)^2 \frac{1}{\cos\theta}\frac{d\theta}{dx} = \frac{1}{r}\frac{\partial}{\partial r}\left\{ r\frac{\tau_x}{\rho}\sin\theta - \frac{r^2}{r_w}\frac{\tau_z}{\rho}\cos\theta \right\}. \qquad (26)$$

---

† More precisely, integrating (19), we should have $P = P_e - \int_y^\delta (\rho W^2/r)\, dy$. However, using the measured profiles of W, it was found that $\int_0^\delta (\rho W^2/r)\, dy < 0{\cdot}05\, \tfrac{1}{2}\rho U_e^2$. Furthermore, since W is maximum at the wall and decreases very rapidly, the significant contributions to the integral $\int_0^\delta (\rho W^2/r)\, dy$ come from the inner region, whereas we are interested here in the outer layer.

If we consider the asymptotic case of small velocity defects, i.e. $(U_e - U)/U_e \ll 1$, we can neglect the term involving $(U_e - U)^2$ in (26). Then a possible solution is

$$(U_e - U) + \frac{r}{r_w}\frac{W}{\tan\theta} = 0, \tag{27a}$$

$$\frac{1}{\sin\theta\cos\theta}\frac{d\theta}{dx} = \frac{1}{U_e}\frac{dU_e}{dx}, \tag{27b}$$

$$\frac{r}{r_w}\tau_x\sin\theta - \frac{r^2}{r_w^2}\tau_z\cos\theta = 0, \tag{27c}$$

where the right-hand side of (27*c*) is obtained by evaluating the constant o integration at the edge of the layer. θ was originally assumed an arbitrary function of x, but (27*b*) now provides an equation for its determination.

From the hodograph diagrams, figures 23 and 24, we see that, after the transitory regime, the observed asymptotic behaviour of the polar velocity profiles in the outer layer verifies solution (27*a*) provided that $\theta = \theta_0$. The correlation between data and (27*a*) appears to hold for $(U_e - U)/U_e \lesssim 0{\cdot}2$ as was assumed in the derivation of (27*a*–*c*). The next data comparison concerns (27*b*), whose solutions can be written as

$$\tan\theta_0/U_e = \text{constant}. \tag{28}$$

Although variations with respect to x of both θ_0 and U_e are small, the data indicate that the ratio (28) is indeed a constant. Finally, we write (27*c*) as

$$\tau_z = \frac{r_w}{r}\tau_x\tan\theta_0. \tag{29}$$

In figure 25, it is shown that the data for $\overline{uv}$ and $\overline{vw}$ are in excellent agreement with (29) in the range where (27*a*) applies. Data from both rotation rates are plotted in figure 25, and it is recalled that θ_0 is very different in both instances.

From the above discussion on the three-dimensional turbulent boundary layer, it is possible to draw some conclusions on the hypothesis of scalar eddy viscosity. The coefficients of effective eddy viscosity ν_e (where $\nu_e = \nu_\tau + \nu$ but $\nu/\nu_\tau \ll 1$) are defined according to

$$\frac{1}{\rho}\tau_x = \nu_{e_x}\frac{\partial U}{\partial r}, \quad \frac{1}{\rho}\tau_z = \nu_{e_z}\left(\frac{\partial W}{\partial r} - \frac{W}{r}\right). \tag{30a,b}$$

In figure 26, the ratio ν_{e_z}/ν_{e_x}, evaluated from the data, is plotted for all x stations and for the two rotation rates. The scatter is obviously large, owing to the combined errors in $\overline{uv}$, $\overline{vw}$, and the numerically computed derivatives. Because of that, we were not able to evidence any trend with respect to x or y, which is why all the points were collected on a single graph. The mean value of the ratio is $0{\cdot}7$ with a standard deviation of the order of 20 %. All the points presented in figure 26 lie outside the inner region (as defined from the polar diagrams), but many of them exceed the domain of validity of (27*a*) and (29). Therefore, strictly speaking, the eddy viscosity is not a scalar property of the turbulent field, at least in the outer region of the present boundary layer. (However, in theories

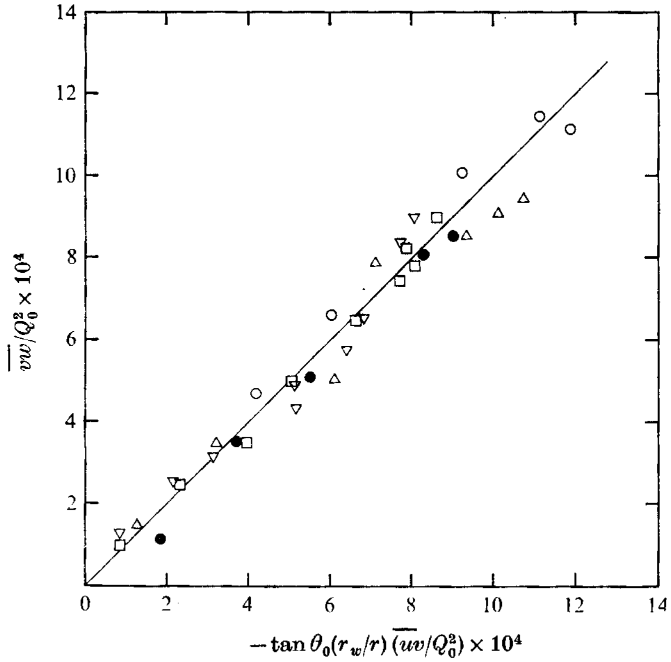

FIGURE 25. Comparison of data with asymptotic polar solution for turbulent stresses in outer region of boundary layer. Data from two rotation rates. ——, (29).

Symbol	Station	$R \times 10^{-4}$	Ω
○	8	4·14	1·8
△	7	4·14	1·8
●	6	4·14	1·8
□	8	7·95	0·936
▽	7	7·95	0·936

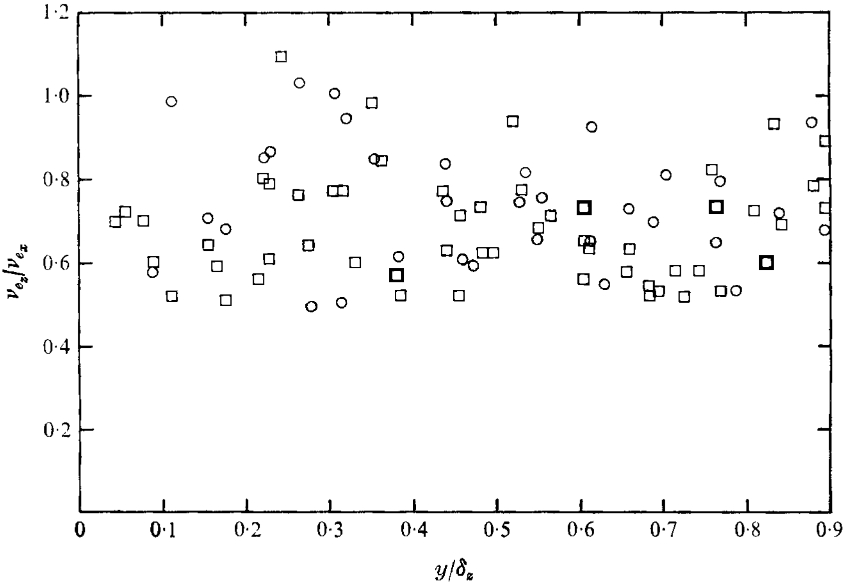

FIGURE 26. Ratio of experimentally measured coefficients of eddy viscosity. δ_z is thickness of circumferential layer.

	$R \times 10^{-4}$	Ω
○	7·95	0·936
□	4·14	1·8

using an eddy viscosity, a value of $\nu_{e_z}/\nu_{e_x} \simeq 0{\cdot}7$ is not terribly far from 1, particularly when it is unity nearer the wall; useful predictions could probably be made by assuming it unity everywhere.) From (27*a, c*) and (30*a, b*) we obtain

$$\frac{\nu_{e_z}}{\nu_{e_x}} = \left(1+\frac{W}{r}\bigg/\frac{\partial W}{\partial r}\right)\bigg/\left(1-\frac{W}{r}\bigg/\frac{\partial W}{\partial r}\right),$$

where experimentally the quantity $(W/r)/(\partial W/\partial r)$ is near $-0{\cdot}1$, so that it generally appears to be in agreement with data of figure 26. For a planar geometry (i.e. $r_w \to \infty$), the condition for a scalar effective eddy viscosity is apparently obtained.

10. Prediction of the wall curvature effect in the law of the wall region

To complete our analysis of the near wall region, we can attempt to predict the radial distributions of the mean velocity components. Equation (23) suggests that the mean rate of strain vector has a constant direction θ_w, independent of y, near the wall. Furthermore, from the definition of θ_w, it is seen that this direction is the same as the wall shear stress vector. We therefore have the following situation in the inner region: a layer of constant direction of mean rate of strain depending only on friction parameters τ_{x_w} and τ_{z_w}. These constitute the well-known conditions for the existence of the law of the wall. In particular, it is not necessary to specify the nature of the outer layer, which in the present case is three-dimensional. Hence, in principle our data should satisfy this classical model.

As suggested by Clauser, the data may be plotted as $\bar{Q}/Q_e$ against $Q_e\bar{y}/\nu$, where $\bar{Q} = (U^2+(W_0+W)^2)^{\frac{1}{2}}$ and Q_e is the free-stream value. In these co-ordinates the law of the wall is a family of curves parametric in C_f. (The variable $\bar{y}$ was used instead of y because this was shown to be the proper choice in the limit of no rotation. However, differences between $\bar{y}$ and y are rather small at these heights.) Although the data on figures 27 and 28 indicate a fairly well-defined semi-logarithmic region, it is impossible to find a skin-friction coefficient that would allow a reasonable fit with a law of the wall curve.

Wall curvature is very likely the factor responsible for this phenomenon. In an attempt to understand the wall curvature effect more fully, we shall consider the equations for the turbulent stresses. Since these equations are not closed, assumptions are required. In §10 we shall investigate the simplest possible assumptions, in an attempt to predict the aforementioned wall curvature effect.

The equations for the turbulent velocity moments are written, in generalized orthogonal co-ordinates, as

$$\begin{aligned}\frac{\partial}{\partial t}\overline{u_iu_j}+(U^k\overline{u_iu_j})_{,k} &= -\overline{u^ku_i}\,U_{j,k}-\overline{u^ku_j}\,U_{i,k}\\ &\quad-\left\{\overline{u^ku_iu_j}+\frac{\delta_i^k}{\rho}\overline{u_jp}+\frac{\delta_j^k}{\rho}\overline{u_ip}-\overline{u_j\frac{\tau_i^k}{\rho}}-\overline{u_i\frac{\tau_j^k}{\rho}}\right\}_{,k}\\ &\quad+\frac{1}{\rho}\overline{pu_{j,i}}+\frac{1}{\rho}\overline{pu_{i,j}}-\frac{1}{\rho}[\overline{\tau_i^ku_{j,k}}+\overline{\tau_j^ku_{i,k}}],\end{aligned} \qquad (31)$$

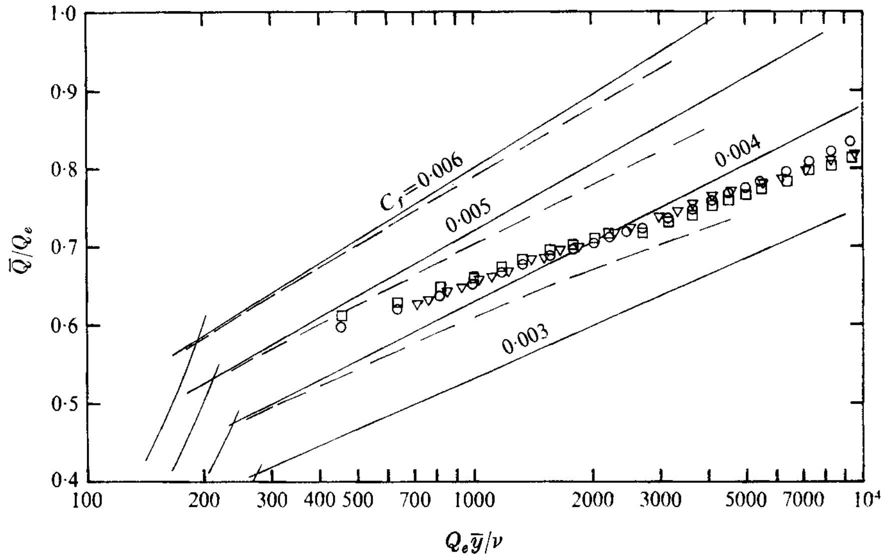

FIGURE 27. Sample profiles showing law of the wall behaviour for $\Omega = 0{\cdot}936$, $R = 7{\cdot}95 \times 10^4$. Stations: ○, 6; □, 7; ▽, 8. ——, Clauser's lines; – – – –, corrected lines of constant C_f obtained from integration of (43).

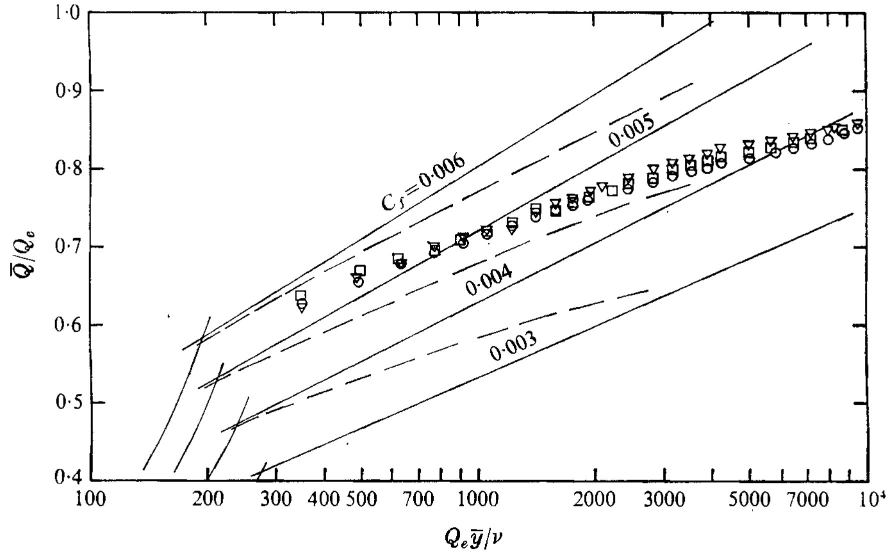

FIGURE 28. Sample profiles showing law of the wall behaviour for $\Omega = 1{\cdot}8$, $R = 4{\cdot}14 \times 10^4$. Symbols and curves as in figure 27.

where $\tau_i^k = \mu g^{kl}(u_{l,i}+u_{i,l})$ and g^{kl} is the metric tensor. The object of the closure approximation consists of writing (31) in terms of $\overline{u_i u_j}$ only. This is done by modelling the different transport terms which involve higher-order moments or correlations of instantaneous velocity gradients. A general framework for this theory was first proposed by Prandtl (1926) and further developed by Rotta (1951). It was later applied to various degrees of generality by Glushko (1965), Beckwith & Bushnell (1968), Mellor & Herring (1968), and Donaldson & Rosenbaum (1968); the particular form used here, the mean turbulent field (MTF) closure, is taken from a survey by Mellor & Herring (1973); the reader is referred to the survey for a full discussion.

The pressure–velocity gradient correlations in (31) redistribute energy among the three components and, on summation over the indices, they vanish identically. They have been called the energy redistribution terms by Rotta, who suggested that

$$\overline{pu_{i,j}}+\overline{pu_{j,i}} = -\frac{\rho q}{3l_1}[\overline{u_i u_j}-\tfrac{1}{3}q^2\delta_{ij}]. \tag{32}$$

The model for the dissipation term is based on the fact that the term is related to small scale turbulence which according to the Kolmogorov hypothesis is isotropic. The dissipation explicitly involves the viscosity and may be defined by $\frac{5}{3}\nu q^2/\lambda^2$, where λ is the Taylor microscale. However, as is well-known (Batchelor 1956), the dissipation is independent of viscosity (away from walls) for sufficiently large Reynolds numbers. In spectral wavenumber space. the dissipation cascade process is determined by small wavenumber inertial processes; the viscosity merely determines the large wavenumber cut-off. We therefore let

$$\overline{\tau_i^k u_{j,k}}+\overline{\tau_j^k u_{i,k}} = 2\frac{\rho q^3}{3\Lambda}g_{ij}. \tag{33}$$

It should also be noted that q^3/Λ may be directly related to the inner asymptote ($r \rightarrow 0$) of the *outer* function for the triple velocity correlation *derivative* in r space as described by the large Reynolds number asymptotic analysis of Mellor (1972) (whereas q^2/λ^2 is related to the second derivative of the *inner* function for the double velocity correlation as $r \rightarrow 0$). The parameters l_1 and Λ are of course empirical length scales. We shall not need to model the diffusion rate; we shall simply represent it by the symbol $\mathscr{D}_{ij}$.

If we invoke the boundary-layer approximation, we obtain for axisymmetric flow

$$\frac{D}{Dt}\overline{u^2}+\mathscr{D}_{11} = -2\overline{uv}\frac{\partial U}{\partial r}-\frac{1}{3}\frac{q}{l_1}(\overline{u^2}-\tfrac{1}{3}q^2)-\frac{2}{3}\frac{q^3}{\Lambda}, \tag{34a}$$

$$\frac{D}{Dt}\overline{v^2}+\mathscr{D}_{22} = 4\overline{vw}\frac{W}{r}-\frac{1}{3}\frac{q}{l_1}(\overline{v^2}-\tfrac{1}{3}q^2)-\frac{2}{3}\frac{q^3}{\Lambda}, \tag{34b}$$

$$\frac{D}{Dt}\overline{w^2}+\mathscr{D}_{33} = -4\overline{vw}\frac{W}{r}-2\overline{vw}\left(\frac{\partial W}{\partial r}-\frac{W}{r}\right)-\frac{1}{3}\frac{q}{l_1}(\overline{w^2}-\tfrac{1}{3}q^2)-\frac{2}{3}\frac{q^3}{\Lambda}, \tag{34c}$$

$$\frac{D}{Dt}\overline{uv}+\mathscr{D}_{12} = 2\overline{uw}\frac{W}{r}-\overline{v^2}\frac{\partial U}{\partial r}-\frac{1}{3}\frac{q}{l_1}\overline{uv}, \tag{34d}$$

$$\frac{D}{Dt}\overline{vw}+\mathscr{D}_{23} = 2(\overline{w^2}-\overline{v^2})\frac{W}{r}-\overline{v^2}\left(\frac{\partial W}{\partial r}-\frac{W}{r}\right)-\frac{1}{3}\frac{q}{l_1}\overline{vw}, \tag{34e}$$

$$\frac{D}{Dt}\overline{uw}+\mathscr{D}_{13} = -2\overline{uv}\frac{W}{r}-\overline{uv}\left(\frac{\partial W}{\partial r}-\frac{W}{r}\right)-\overline{vw}\frac{\partial U}{\partial r}-\frac{1}{3}\frac{q}{l_1}\overline{uw}. \tag{34f}$$

Since we mean to analyse only the law of the wall outside the viscous sublayer and far enough from the separation line between unskewed and skewed flow, it is possible to neglect diffusion (Laufer 1953) and advection in these equations. Similarly, we can write the approximate mean momentum equations in a form valid in the near-wall region:

$$-\frac{r}{r_w}\overline{uv} = \frac{1}{\rho}\tau_{x_w}(x), \quad -\frac{r^2}{r_w^2}\overline{vw} = \frac{1}{\rho}\tau_{z_w}(x). \tag{35a,b}$$

With the left-hand-side terms neglected and $W/r = 0$, (34*a*–*f*) can easily be solved to obtain the classical mixing length or scalar eddy viscosity formulae. However, for $W/r \neq 0$, the algebra becomes extraordinarily complicated (yet the equations are undoubtedly a simplified description of real turbulence). An expansion in the parameter

$$\epsilon \equiv \frac{W}{r}\left(\frac{\partial W}{\partial r}\right)^{-1} \tag{36}$$

is certainly possible, but we find that in our case the value $\epsilon \simeq -0{\cdot}1$ is still not sufficiently small to permit truncation to $O(\epsilon)$. We must, therefore, present full solutions. They are written so that the reader may easily obtain simple asymptotic expressions as $\epsilon \rightarrow 0$.

It is convenient to define

$$\phi \equiv \frac{3l_1}{q}\frac{\partial W}{\partial r}. \tag{37}$$

Using (34*b*, *c*, *f*), (34*d*) and (34*e*) may be written as

$$\overline{uv} = -\overline{v^2}\frac{3l_1}{q}\frac{\partial U}{\partial r}f_1(\epsilon,\phi), \tag{38a}$$

$$\overline{vw} = -\overline{v^2}\frac{3l_1}{q}\frac{\partial W}{\partial r}f_2(\epsilon,\phi), \tag{38b}$$

where

$$f_1(\epsilon,\phi) = \frac{1+2\epsilon\phi^2+14\epsilon^2\phi^2}{(1+2\epsilon\phi^2+2\epsilon^2\phi^2)(1+4\epsilon\phi^2+12\epsilon^2\phi^2)}, \tag{39a}$$

$$f_2(\epsilon,\phi) = \frac{1-\epsilon}{1+4\epsilon\phi^2+12\epsilon^2\phi^2}, \tag{39b}$$

so that $f_1(0,\phi), f_2(0,\phi) = 1$. If we define $\tan\theta \equiv (\partial W/\partial r)/(\partial U/\partial r)$ and use (35*a*, *b*) and (38*a*, *b*) we obtain

$$\tan\theta = \frac{\tau_{z_w}}{\tau_{x_w}}\frac{r_w}{r}\frac{f_1}{f_2}, \tag{40}$$

where, in general, $\theta = \theta(x,r)$. Although not obvious, a two-term expansion $f_1/f_2 \simeq 1+\epsilon+(12\phi^2+1)\epsilon^2$ agrees quite well with the full expression in the range of experimental interest; in fact, f_1/f_2 is quite close to unity. Since $1 \leqslant r/r_w \leqslant 1{\cdot}03$, we have $\tan\theta \simeq \tau_{z_w}/\tau_{x_w} \equiv \tan\theta_w(x)$.

A useful expression relating $\overline{v^2}$ and q^2 is obtained from (34*b*) using (38*b*),

$$\frac{\overline{v^2}}{q^2} = 3\alpha\frac{l_1}{\Lambda}[1+4\epsilon\phi^2 f_2]^{-1}, \tag{41}$$

where $\alpha \equiv \Lambda/9l_1 - \frac{2}{3}$ is a repeatedly useful identity. Furthermore, summing (34*a*–*c*) and using (37), (38*a*, *b*) and (41), we obtain

$$\phi^2 = \frac{\sin^2\theta}{\alpha}\left[\frac{f_1\cos^2\theta+(1-\epsilon)f_2\sin^2\theta}{1+4\epsilon\phi^2 f_2}\right]^{-1}. \tag{42}$$

An expression for the total stress $\tau/\rho \equiv \{(-\overline{uv})^2+(-\overline{vw})^2\}$ may now be obtained from (38*a*, *b*), (41) and (42). Thus,

$$\frac{\tau}{\rho} = \alpha^{\frac{3}{2}}\frac{(3l_1)^3}{\Lambda}\left(\frac{\partial\bar{Q}}{\partial r}\right)^2\left[\left(\frac{f_2}{1+4\epsilon\phi^2 f_2}\right)^3\left(\frac{f_1}{f_2}\cos^2\theta+(1-\epsilon)\sin^2\theta\right)\left(\frac{f_1^2}{f_2^2}\cos^2\theta+\sin^2\theta\right)\right]^{\frac{1}{2}}. \tag{43}$$

It should be noted that in (41)–(43) the expressions in square brackets are the curvature correction factors, which approach unity as $\epsilon \rightarrow 0$.

It is now our plan to integrate (43) numerically for the region close to the wall but outside the viscous region where $\tau = \tau_w$. First, however, Λ and l_1 must be specified. Since the proposed closure model is meant to be universal, we let $\epsilon \rightarrow 0$ and use two-dimensional data to determine the relevant constants. We assume the usual 'mixing length' scaling such that

$$l_1 = Ay, \quad \Lambda = By, \tag{44a, b}$$

where A and B are constants. It is easy to show that (44*a*, *b*) lead to the classical logarithmic result when $\epsilon = 0$. Our principal assumption here is that (44*a*, *b*) are universal in the sense of being independent of curvature effects. Therefore, from (43) we deduce that

$$\alpha^{\frac{3}{2}}\frac{(3l_1)^3}{\Lambda} = \alpha^{\frac{3}{2}}\frac{(3A)^3}{B}y^2 = \kappa^2 y^2, \tag{45a}$$

where κ is the von Kármán's constant, equal to 0·41. Similarly, α can be obtained from two-dimensional results, since, for $\epsilon = 0$, (41) may be written as

$$\overline{v^2}/q^2 = \frac{3\alpha l_1}{\Lambda} = \frac{\alpha}{3\alpha+2}. \tag{45b}$$

From a survey of classical two-dimensional data, we find that $\overline{v^2}/q^2$ is approximately constant in the law of the wall region and lies somewhere around 0·15†.

---

† According to the asymptotic analyses of Yajnik (1970) and Mellor (1972), the outer asymptotes of the inner functions describing the turbulent stress approach constants (while the mean velocity approaches the familiar semi-logarithmic asymptote). From Laufer's (1953) data we find that $\overline{v^2}/q^2 = 0{\cdot}10, 0{\cdot}16$ when $yu_\tau/\nu = 28, 280$, whereas, from the smaller Reynolds number data of Klebanoff (1955), we obtain $\overline{v^2}/q = 0{\cdot}10,\ 0{\cdot}17$ when $yu_\tau/\nu = 25, 85$. However, data are represented by composite, inner and outer functions and the larger quoted values of yu_τ/ν are where we estimate that the outer (defect) function begins to dominate.

Using this number, we have $\alpha = 0{\cdot}55$. Finally, as an expedient (and as it will turn out, an incorrect) measure, we evaluate the constant of integration by assuming it equal to the classical value at $\epsilon = 0$. On Clauser-type plots we thus obtain a family of solutions for the mean velocity, valid in the near wall region outside the viscous sublayer. Sample cases are illustrated in figures 27 and 28 for different choices of the skin-friction coefficient C_f; the parameter θ_w was evaluated from the hodograph diagrams. This permits a comparison of the data and the corresponding two-dimensional solutions.

It is seen that the corrections are in the proper direction. The slopes of the lines of constant C_f are significantly smaller than their two-dimensional counterparts and agree better with the general behaviour of the experimental points. However, using these solutions to evaluate C_f, it is found that the numbers obtained in this manner are consistently 20–25 % larger than those reported in table 2. A plausible explanation for this difficulty resides in our choice of the inner boundary condition for the integration of (43), where we assumed that the viscous sublayer was not altered by the curvature effect. If indeed the constants of integration were to be changed to reach agreement with the C_f presented in table 2, we can see in figures 27 and 28 that the solutions of (43) would reproduce even better the experimental results, since a small C_f corresponds to greater reduction in the slope.

In summary, these approximate solutions, as obtained here, cannot be given full quantitative significance because there is a lack of definite information concerning the viscous sublayer, or equivalently the inner boundary condition. However, qualitatively, they constitute a fair prediction of the observed phenomenon (i.e. a non-negligible reduction, in comparison with two-dimensional flows, of the slope of the mean velocity profiles). It can be easily seen by following the derivation of (43) that the corrections are primarily a consequence of additional turbulent energy production proportional to W/r, hence the expression 'curvature effects.'

A significant point concerning these solutions is that, except for the usual approximation of neglecting advection and diffusion in the MTF turbulent transport equations, they were obtained from the full MTF equations with no empiricism save that required in plane, two-dimensional flow. For this experiment, similar results could probably have been obtained by modelling directly the destabilizing effects of the centrifugal forces. Such an analysis is reported in Cham & Head (1970), where the increase in mixing length is expressed as a linear function of an analogous Richardson number defined as the ratio of the square of the Brunt–Väisälä frequency to the square of the turbulence frequency. However, we believe that the approach of the present paper is more general, inasmuch as the necessary empirical constants are evaluated independently of a particular geometry. Thus, the physics of the centrifugal instability is built-in in the MTF model and no further assumptions are required.

Based on these observations, we conclude that the MTF closure appears to represent properly the physics of the interaction between turbulent energy budget and mean velocity field. Hence, it is expected that the method will work well in problems involving different processes for production of additional turbulent energy.

11. Dynamics of turbulence

Prediction of mean velocity field, as was discussed in § 10, is not necessarily a guarantee that the modelling of each dynamical process is physically correct. This constitutes the real difficulty or danger connected with the construction of any closure theory. The problem is best seen by examination of (38*a*, *b*), which closely resemble the classical mixing length relation, owing to our neglect of advection or 'history'. It is quite probable that simple closure hypotheses of this type would lead to accurate enough solutions, even in this rapidly developing flow. In fact, the constitutive hypotheses could conceivably be wrong and the model still work well so long as the above condition on rapid response or negligible 'history' is satisfied. It is thus important to seek further experimental information, to check whether the individual modellings do approximate the corresponding physical processes.

This is a very difficult task, because measurement of all the terms involved in the turbulent transport equations is either too complex or simply beyond existing experimental techniques. Except for advection and production, it is impossible, in most practical cases, to discuss separately and exactly the various other rates of the energy processes: turbulent and viscous diffusion, redistribution and dissipation. Most often one must satisfy oneself with qualitative or approximate representations based on the knowledge of the end effect, i.e. the spatial gradients of the turbulent stress components. For example, many turbulent shear flows are termed equilibrium flows from the observation that the turbulent energy level varies slowly along the streamlines with only a gentle gradient transversely. Hence, it is argued that advection and diffusion are negligibly small, whereas locally the dissipation rate balances the production rate almost exactly. In the present experiment, we have a situation where this equilibrium is suddenly upset by a near step increase in the straining rate. Studying the turbulent stress components as the fluid particles move across this rapid perturbation, it is hoped that additional information might be gained concerning the rates of redistribution, diffusion and dissipation.

The situation is illustrated in figures 29 and 30, where the projections on a meridional plane of estimated streamline surfaces are drawn, along with various boundary-layer thicknesses. Curve (iii) represents the thickness of the transverse layer (velocity component W), and thus constitutes a boundary between a region of unskewed and a region of skewed flow. From data evaluation, it is found that the change in the $\partial W/\partial r$ rate of strain is very rapid: the total rise takes place within a boundary-layer thickness. Hence, as it travels along streamlines, the turbulent fluid experiences a steep increase in energy input. There follows a readjustment whose nature and speed are indicative of the various rates of the energy processes.

Dynamics of energy redistribution

The energy data $\overline{u^2}$, $\overline{v^2}$, $\overline{w^2}$ and q^2 are plotted against x for three different values of the normal co-ordinate y (figures 31 and 32). As is shown in figures 29 and 30, lines of constant y nearly approximate the streamlines. Thus, the experimental

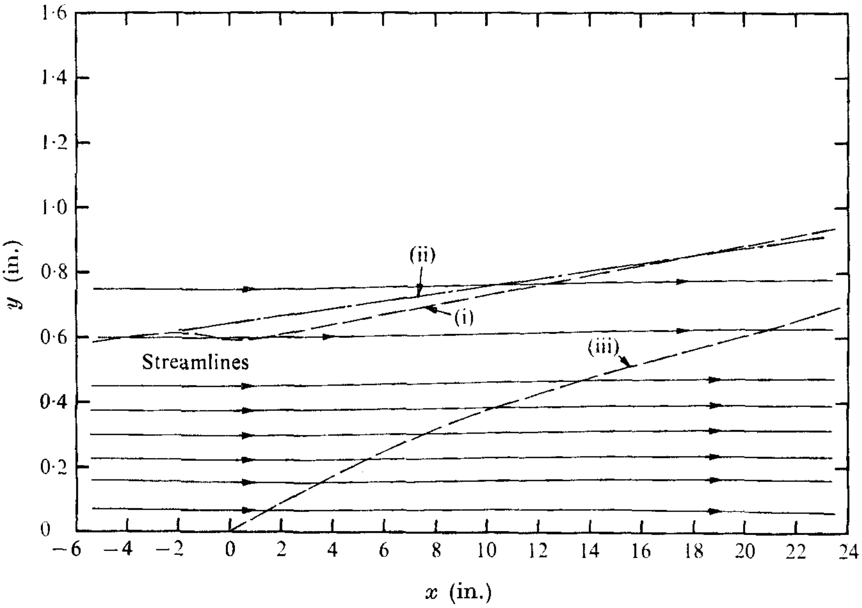

FIGURE 29. Qualitative pictures of the flow field for $\Omega = 0{\cdot}936$, $R = 7{\cdot}95 \times 10^4$. (i) Overall boundary-layer thickness, with rotation; (ii) overall boundary-layer thickness, without rotation; (iii) thickness of the transverse layer δ_z.

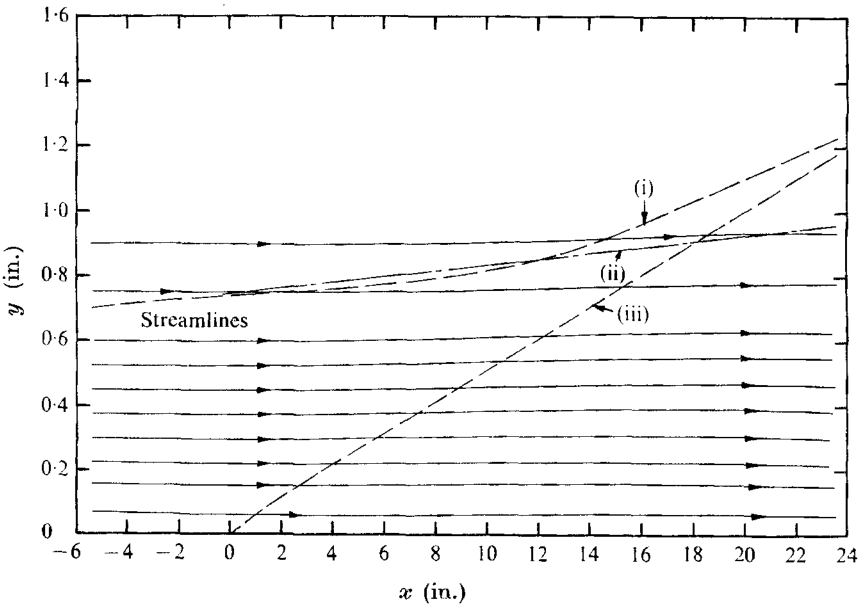

FIGURE 30. Qualitative picture of flow field for $\Omega = 1{\cdot}8$, $R = 4{\cdot}14 \times 10^4$.
(i), (ii), (iii) as in figure 29.

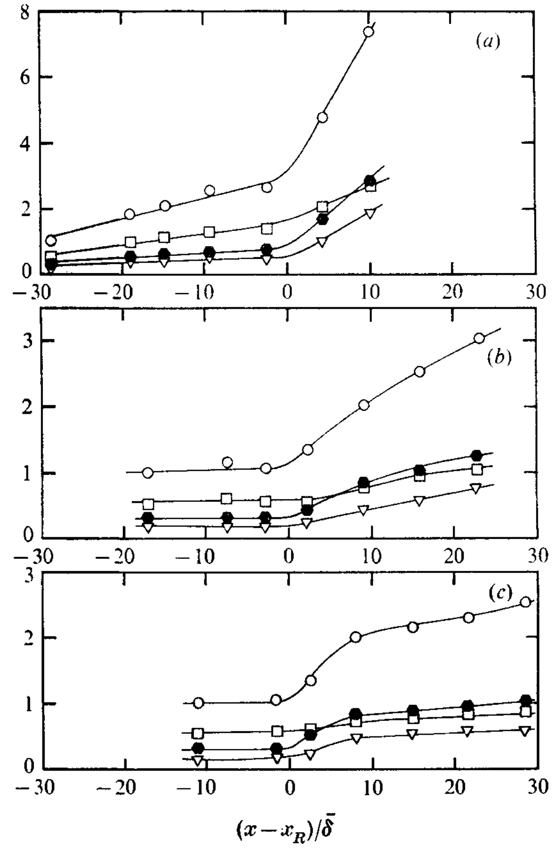

FIGURE 31. Distribution of turbulent energy components along streamlines defined by lines of constant y for $\Omega = 0{\cdot}936$, $R = 7{\cdot}95\times10^4$, ○, q^2/q_1^2; □, $\overline{u^2}/q_1^2$; ▽, $\overline{v^2}/q_1^2$; ●, $\overline{w^2}/q_1^2$. y: (a) 0·5, (b) 0·3, (c) 0·1 in.

curves drawn in figures 31 and 32 represent very closely the evolution of the turbulent energy components along streamlines. To exemplify the relative growth in each case, the data are normalized by the value of the turbulent energy at station 1, q_1^2. The abscissa is $(x-x_R)/\bar{\delta}$, where x_R is defined as the intersection of the line y = constant with curve (iii) of figure 29 or 30. Hence, $x = x_R$ is the location where the approximate step input is applied. $\bar{\delta}$ is the overall boundary-layer thickness averaged over the total available length.

The first terms on the right sides of (34*a*–*f*) are the production rates of turbulent energy, and constitute the inputs in the equations for the components of the Reynolds stress tensor. It is recalled that, except for the boundary-layer approximation, these terms are exact. While all the rates of strain in these expressions undergo a rapid change, numerical evaluation from the data shows that by far the largest and steepest change occurs in $\partial W/\partial r$. Therefore, the sudden increase in energy production is initially concentrated in the energy component $\overline{w^2}$; data indicate that it is approximately an order of magnitude smaller for $\overline{u^2}$ and $\overline{v^2}$. However, inspection of figures 31 and 32 shows that the three energy components

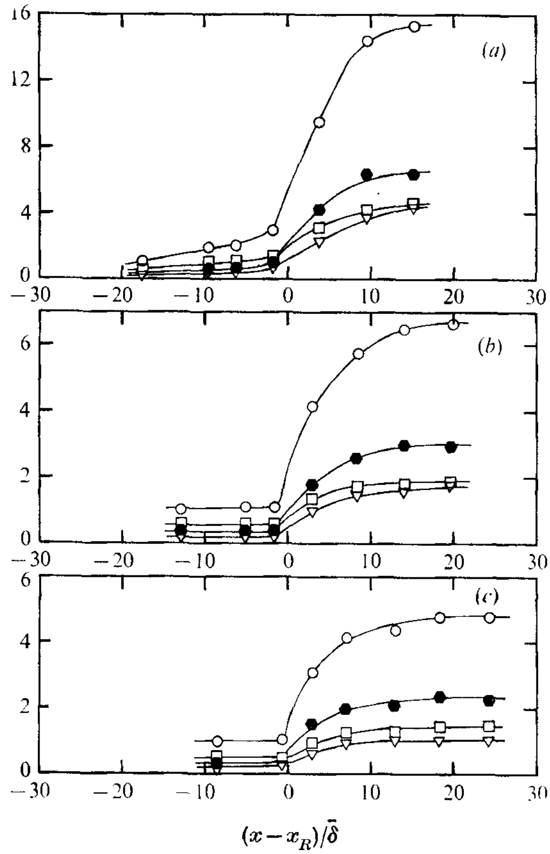

FIGURE 32. Distribution of turbulent energy components along streamlines defined by lines of constant y for $\Omega = 1{\cdot}8$, $R = 4{\cdot}14 \times 10^4$. Symbols as in figure 31. y: (a) 0·5, (b) 0·3, (c) 0·1 in.

start increasing at the same point, although as expected the rise in $\overline{w^2}$ is faster. Hence, there must be an energy supply in $\overline{u^2}$ and $\overline{v^2}$ other than direct production. The most probable mechanism for this is the redistribution of energy among the components through the energy redistribution terms (the pressure–velocity gradient correlations). Not only is the process responsible for e.g. direct input in $\overline{u^2}$ but, by also contributing to $\overline{uv}$, it indirectly increases the $\overline{u^2}$ production. Within the limits of the present experiment, the results on figures 31 and 32 exhibit no measurable lag between the growth of the individual energy components. In other words, the readjustment of the relative magnitudes of the three turbulent energy components is completed very quickly. Therefore, on the basis of these measurements, it is concluded that the process of energy redistribution responds very rapidly to an applied straining motion.

Dynamics of energy production, advection and dissipation

The processes of energy production, advection and dissipation evidently constitute another very important dynamical aspect of (31). Since the redistribution terms vanish exactly in the equation for the total turbulent kinetic energy, it is convenient to study the development of q^2 alone, which is governed by the balance between production, advection, diffusion and dissipation. It is the purpose of the following analysis to extract from our measurements as much information as possible concerning these individual rates.

The available data are sufficient to compute directly the turbulent energy production rate. Performing this calculation along a streamline, it is found that, in a large portion of the flow field far enough from the wall, the production rate rises sharply, within a boundary-layer thickness, to a much higher level and remains reasonably constant thereafter. Hence, to simplify the discussion, we postulate a streamwise step function for the turbulent energy input. Similarly the q^2 advection rate may be easily calculated from the slope of the q^2 curves in figures 31 and 32. Qualitatively, it is observed that the advection rate is initially very small, that it increases abruptly to a maximum at the onset of the distortion, that it starts decreasing almost immediately after, and that it continues to decrease over a measurable distance before it becomes negligible again. (In the case of the largest mainstream velocity, figure 31, the available length is not long enough clearly to evidence this asymptotic behaviour.)

From these observations concerning the rates of production and advection, it may be argued that the turbulent processes of diffusion and dissipation react promptly but smoothly to the step-like production increase before dissipation can finally reach a value closely in balance with production. In the conditions of the present experiment, this 'history' manifests itself over a distance of the order of 20 boundary-layer thicknesses in the lower velocity case, whereas the corresponding length is greater than 30δ in the high velocity case.

To arrive at a somewhat more quantitative description, it is necessary to introduce hypotheses. We choose here the framework of the MTF closure model described earlier; it is hoped that this approach will help us understand the important processes governing the observed data. By definition,

$$q^2 = \overline{u^i u_i} = g^{ij}\overline{u_i u_j}.$$

Thus, upon multiplying (31) by g^{ij}, one obtains

$$\frac{\partial}{\partial t}q^2 + (U^k q^2)_{,k} = -\left\{\overline{u^k u^l u_l} + \frac{2}{\rho}\overline{u^k p} - \frac{2}{\rho}\overline{u^l \tau_l^k}\right\}_{,k} - 2\overline{u^k u^l}\,U_{l,k} - \frac{2}{\rho}\overline{\tau_l^k u^l_{,k}}. \qquad (46)$$

Note again that the redistribution terms are identically zero in (46).

We introduce here an important simplification: we postulate that diffusion is negligible. Although these terms are generally small in near equilibrium flows, there is no guarantee that such is the case in the present situation; however, we use it here as a starting point to be reviewed *a posteriori*. The simplified equation (46) may then be written schematically as

$$\frac{D}{Dt}(\tfrac{1}{2}q^2) = P - D, \qquad (47)$$

where $$P = -\overline{u^k u_l}\, U_{l,k}, \quad D = \frac{1}{\rho}\overline{\tau_l^k u^l_{,k}}$$

represent respectively the production and the dissipation rates. The left-hand side is the rate of change of q^2 along a streamline. However, in figures 29 and 30 it is shown that the streamlines are nearly parallel to the wall surface. Hence, we can rewrite (47) as

$$\tfrac{1}{2}U\frac{d}{dx}(q^2) + D = P, \tag{48}$$

where U is the local mean flow velocity, which is approximately constant along a streamline. For the dissipation D, we use the MTF model defined in (33), i.e.

$$D = q^3/\Lambda, \tag{49}$$

which here may be simply considered as a defining relation for the empirical length scale Λ. Λ is assumed constant in the outer region of the turbulent boundary layer. Finally, as has been established earlier, P may be approximated by a step function which passes from a level P_I to a level P_F. If one non-dimensionalizes (48) after substituting for D, one obtains for $x > x_R$

$$dh/d\eta + h^{\frac{3}{2}} = 1, \tag{50}$$

where $$h = (q/q_F)^2, \quad \eta = 2(x - x_0)/\Lambda. \tag{51a,b}$$

q_F^2 is the downstream energy level attained asymptotically as $x \to \infty$, and it is defined by $q_F^3 = P_F\Lambda$. Equation (50) is easily solved numerically; a convenient boundary condition is $h(0) = 0$. Finally, x_0 may be calculated from

$$h(\eta_R) = q_I/q_F, \tag{52}$$

where $\eta_R = 2(x_R - x_0)/\Lambda$, and where q_I^2 is the energy level measured on the given streamline prior to the beginning of the distortion.

In figure 33, we compare the data of figures 31 and 32 with the numerical solution of (50) in the cases where q_F, q_I and x_0 can be unambiguously determined. The four different sets of data were brought to coincide with the theoretical curve by choosing

$$\Lambda/\overline{\delta} = 3{\cdot}5 \mp 0{\cdot}3. \tag{53}$$

Hence, the trend of the data seems to indicate that $\Lambda/\overline{\delta}$ is independent of Reynolds number and rotation rate far enough from the wall. This result apparently corroborates the assumption made in constructing the dissipation model. However the value quoted in (53) is approximately twice the value obtained by equating production and dissipation in equilibrium situations. The latter calculation is performed by direct substitution in

$$\Lambda = q^3/P. \tag{54}$$

The value $$\Lambda/\overline{\delta} = 1{\cdot}4 \mp 0{\cdot}3 \tag{55}$$

was computed from measurements in the outer boundary layer of the no-rotation case, in the flow regions preceding the distortion in both rotation cases, and finally in the asymptotic downstream region of the highest rotation rate case.

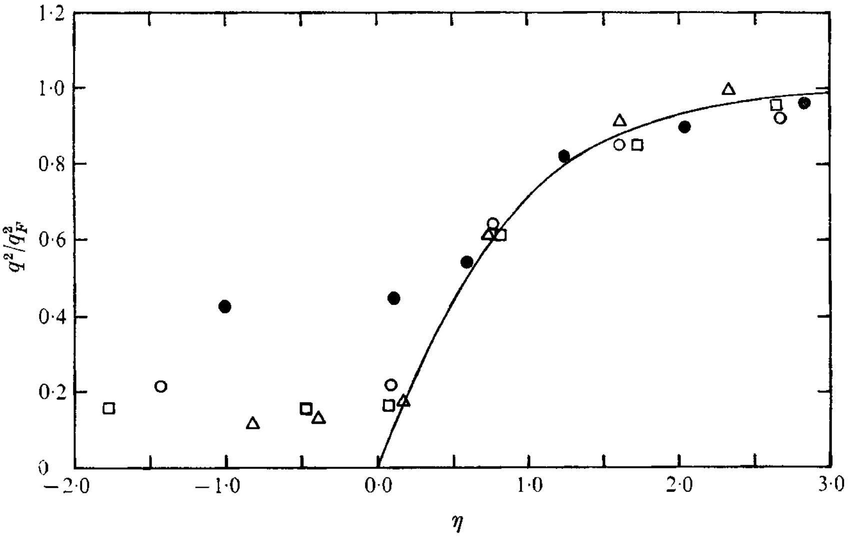

FIGURE 33. Comparison of data with theory for the distribution of the turbulent kinetic energy along streamlines defined by lines of constant y. ——, numerical solution of (50), with boundary condition $h(0) = 0$.

	$R \times 10^4$	Ω	y (in.)
○	4·14	1·8	0·1
□	4·14	1·8	0·3
△	4·14	1·8	0·5
●	7·95	0·936	0·1

That the value of Λ is larger in the rapid adjustment region than in the upstream and downstream near equilibrium region is understandable, in view of the fact that we have approximated the production term as a step function and diffusion has been neglected to simplify the analysis. In the adjusting region, it is reasonable to believe that the high turbulent energy gradients observed along the relatively thin region between unskewed and skewed fluid give rise to significant outward diffusion. Inclusion of this effect would signify replacing the step function production term in (48) with a more smoothly increasing 'production minus diffusion' term. By tracing through the above analysis, it may be seen qualitatively that this change would result in a smaller value of Λ relative to the value given in (53).

The magnitude of the difference between (53) and (55) suggests that diffusion grows to the same order as dissipation during the rapid straining motion. Hence, a full solution to the system (34*a*–*f*) including a diffusion model would be required to achieve any kind of precision. However, in light of the results illustrated in figure 33, it is probable that the basic length scale Λ which characterizes the dissipation process is relatively constant compared with the observed changes in q^2 and the other flow properties.

In summary, we can draw the following qualitative picture of the turbulence dynamics. On the one hand, through the action of the redistribution processes, the structure of turbulence seems to adjust itself very rapidly to local changes. This partly explains the success of the various eddy viscosity type closure theories since the above constitutes a necessary condition for their existence. It also indicates why the latter type of behaviour must be dominant in any higher-order model. On the other hand, the slower approach toward production–dissipation equilibrium implies that turbulence has non-negligible history as far as its intensity is concerned.

12. Conclusions

It was found that the axially rotated cylinder constitutes a relatively simple means of studying three-dimensional boundary layers. A technique was developed for complete mean velocity and turbulence measurements in skewed flows. The method permits measurements of all six components of the $\overline{u_i u_j}$ tensor; it requires no prior knowledge of the local mean flow angle, and the angular calibration of the sensor is a built-in feature. However, some difficulties were experienced with the stress data $\overline{uv}$ and $\overline{vw}$ near the wall surface because of probe size by comparison with the scale of the skewed flow in that region. A corrected method of interpretation was used to account for this effect. Comparison with the values of $\overline{uv}$ and $\overline{vw}$ obtained from the momentum equations corroborates these results.

The hodograph diagrams of the mean velocity vectors revealed the existence of two characteristic regions in the flow field. In the near wall region, it was observed for all cases considered in this experiment that the mean rate of strain vectors assumed a constant direction equal to that of the wall shear stress vector. In a rotating frame of reference, this means that the mean velocity vectors are collateral. Theoretically, this behaviour is easily predictable from the Navier–Stokes equations in the limit $y \to 0$. However, to explain the observation that this condition exists at relatively large values of y, it was sufficient to postulate a scalar effective eddy viscosity.

As y becomes larger the situation described above ceases to be valid; in a rotating frame of reference the mean flow angle begins to vary with distance from the wall. However, as the flow develops downstream and the transverse layer (velocity component W) begins to reach the edge of the overall boundary layer, the hodograph diagrams showed that the outer region is characterized by a constant direction of the vector $\mathbf{V} = U\mathbf{i} + (W_0 + r/r_W)\mathbf{k}$. Theoretically, it was demonstrated that this behaviour constitutes an asymptotic solution, valid for small velocity defects, to the equations of mean motion. This solution includes a relation between $\overline{uv}$ and $\overline{vw}$, which was confirmed experimentally. Interestingly, the two separate solutions for the mean velocity vector and the stress vector can be combined to show that the eddy viscosity is not a scalar in the outer region. The above prediction was further corroborated by experimental evaluation of the ratio ν_{e_z}/ν_{e_x}, which was found to be 0·7. Although this number is not terribly far from unity, it was concluded that, in principle, the effective eddy viscosity cannot be considered a scalar property of turbulent fluids. In the present case, streamline curvature is probably the factor responsible, whereas an eddy viscosity may very well be realized in plane flow.

Although the basic requirements for its existence were realized, the mean flow data did not satisfy the universal form of the law of the wall, a fact which is attributed to a curvature effect which is responsible for additional turbulent energy production. Using a simplified version of the higher-order MTF closure (Mellor & Herring 1973), which requires no empiricism over that required for plane flow, a fair prediction of this effect was achieved. Because of its generality, it is very possible that this approach will contribute to the study of problems involving different physical processes of turbulent energy production such as stratified flow problems.

In the discussion of turbulence response to rapidly changing mean rate of strain, it was found that the redistribution processes react promptly to realign the turbulence structure. Similarly, the dissipation and the diffusion rates increase rapidly, to balance the sudden rise in energy production. However, the return to production–dissipation equilibrium is slower; advection remains important for several boundary-layer thicknesses following the applied straining motion. The present experiment constitutes a relevant test of closure theories dealing with the turbulent transport equations. In particular, our findings emphasize the special attention that must be given to the modelling of the redistribution processes. Owing to their effectiveness in rapidly adjusting the turbulence structure to local mean flow conditions, they play a decisive role in the turbulent energy budget.

This research was begun under sponsorship of the Air Force Office of Scientific Research, contract AF 49(638)-1656. The work was completed with the support of the Air Force Office of Scientific Research under contract AFOSR-70-1828, directed by Major Donald L. Calvert. One of the authors (L.R.B.) expresses his gratitude to La Compagnie Hydro-Québec for financial support during a significant part of this research.

REFERENCES

Batchelor, G. K. 1956 *The Theory of Homogeneous Turbulence.* Cambridge University Press.

Batchelor, G. K. & Proudman, I. 1954 The effect of rapid distortion of a fluid in turbulent motion. *Quart. J. Mech. Appl. Math.* **7**, 83.

Beckwith, I. E. & Bushnell, D. M. 1968 Calculation of mean and fluctuating properties of the incompressible turbulent boundary layer. *Proc. Computation of Turbulent Boundary Layers, AFOSR IFP Stanford Conference, Mech. Eng. Dept., Stanford University*, vol. 1, p. 275.

Bissonnette, L. R. 1970 An experimental study of the development of a three-dimensional turbulent boundary layer under rapidly changing rate of strain. Ph.D. thesis, Department of Aerospace and Mechanical Sciences, Princeton University.

Bradshaw, P. & Terrell, M. G. 1969 *N.P.L. Aero. Rep.* no. 1305.

Cham, T.-S. & Head, M. R. 1969 Turbulent boundary-layer flow on a rotating disk. *J. Fluid Mech.* **37**, 129.

Cham, T.-S. & Head, M. R. 1970 The turbulent boundary layer on a rotating cylinder in an axial stream. *J. Fluid Mech.* **42**, 1.

Champagne, F. H., Sleicher, C. A. & Wehrman, O. H. 1967 Turbulence measurements with inclined hot-wires. *J. Fluid Mech.* **28**, 153.

Clauser, F. H. 1954 Turbulent boundary layers in adverse pressure gradients. *J. Aero. Sci.* **21**, 91.

DONALDSON, C. DU P. & ROSENBAUM, H. 1968 Calculation of the turbulent shear flows through closure of the Reynolds equations by invariant modeling. *ARAP Rep.* no. 127.

FUJITA, H. & KOVASZNAY, S. G. 1968 Measurements of Reynolds stress by a single rotated hot wire anemometer. *Rev. Sci. Instrum.* **39**, 1351.

FURUYA, Y., NAKAMURA, I. & KAWACHI, H. 1966 The experiment on the skewed boundary layer on a rotating body. *Bulletin JSME*, **9**, 702.

GLUSHKO, C. S. 1965 Turbulent boundary layer on a flat plate in an incompressible fluid. *N.A.S.A.* TT-F-10, 080.

HERRING, H. J. & NORBURY, J. F. 1967 Some experiments on equilibrium turbulent boundary layers in favourable pressure gradients. *J. Fluid Mech.* **27**, 541.

HORNUNG, H. G. & JOUBERT, P. N. 1963 The mean velocity profile in three-dimensional turbulent boundary layers. *J. Fluid Mech.* **15**, 368.

JOHNSTON, J. P. 1960 On the three-dimensional turbulent boundary layer generated by secondary flow. *Trans. A.S.M.E.* D **82**, 233.

JOHNSTON, J. P. 1970 Measurements in a three-dimensional turbulent boundary layer induced by a swept, forward-facing step. *J. Fluid Mech.* **42**, 823.

KLEBANOFF, P. S. 1955 Characteristics of turbulence in a boundary layer with zero pressure gradient. *N.A.C.A. Rep.* no. 1247.

LAUFER, J. 1953 The structure of turbulence in fully developed pipe flow. *N.A.C.A. Tech. Note*, no. 2954.

MELLOR, G. L. 1972 The large Reynolds number asymptotic theory of turbulent boundary layers. *Int. J. Eng. Sci.* **10**, 851.

MELLOR, G. L. & GIBSON, D. M. 1966 Equilibrium turbulent boundary layers. *J. Fluid Mech.* **37**, 129.

MELLOR, G. L. & HERRING, H. J. 1968 Two methods of calculating turbulent boundary layer behaviour based on numerical solutions of the equations of motion. I. Mean velocity field method; II. Mean turbulent field method. *Proc. Computation of Turbulent Boundary Layers, AFOSR IFP Stanford Conference, Mech. Eng. Dept., Stanford University*, vol. 1, p. 331.

MELLOR, G. L. & HERRING, H. J. 1973 A survey of the mean turbulent field closure models. *A.I.A.A. J.* **11**, 590.

MOFFATT, H. K. 1965 The interaction of turbulence with rapid uniform shear. *Aero. Dept., Stanford University, Rep. AFOSR*-65-1795.

PATEL, R. P. 1963 Measurements of the Reynolds stresses in a circular pipe as a means of testing a DISA constant temperature hot-wire anemometer. *Mech. Eng. Res. Lab., McGill University, Tech. Note*, no. 63–6.

PATEL, R. P. 1968 Reynolds stresses in fully developed flow down a circular pipe. *Mech. Eng. Res. Lab., McGill University, Rep.* no. 68–7.

PERRY, A. E. & JOUBERT, P. N. 1965 A three-dimensional turbulent boundary layer. *J. Fluid Mech.* **22**, 285.

PRANDTL, L. 1926 *Proc. 2nd Int. Cong. Appl. Mech., Zurich.*

PROBSTEIN, R. F. & ELLIOT, D. 1956 The transverse curvature effect in compressible axially symmetric laminar boundary layer flow. *J. Aero. Sci.* **23**, 208.

RIBNER, H. S. & TUCKER, M. 1952 Spectrum of turbulence in a contracting stream. *N.A.C.A. Tech. Note*, no. 2606.

RICHMOND, R. L. 1957 Experimental investigation of thick, axially symmetric boundary layers on cylinders at subsonic and hypersonic speeds. *Guggenheim Aero. Lab., California Institute of Technology, Memorandum* no. 39.

ROTTA, J. C. 1951*a* Stratische Theorie Nichthomogener Turbulenz. *Z. Phys.* **129**, 547.

ROTTA, J. C. 1951*b* Stratische Theorie Nichthomogener Turbulenz. *Z. Phys.* **131**, 51.

SANDBORN, V. A. 1955 Experimental evaluation of momentum terms in turbulent pipe flow. *N.A.C.A. Tech. Note*, no. 3266.

TOWNSEND, A. A. 1954 The uniform distortion of homogeneous turbulence. *Quart. J. Mech. Appl. Math.* **7**, 104.

YAJNIK, K. S. 1970 Asymptotic theory of turbulent shear flows. *J. Fluid Mech.* **42**, 411.

YU, Y.-S. 1958 Effect of transverse curvature on turbulent boundary layer characteristics. *J. Ship Res.* **12**, 33.